The Astrophysical Journal, 945:128 (17pp), 2023 March 10 https://doi.org/10.3847/1538-4357/acb931

VLA Legacy Survey of Molecular Gas in Massive Star-forming Galaxies at High Redshift

Marta Frias Castillo[1], Jacqueline Hodge[1], Matus Rybak[1,2], Paul van der Werf[1], Ian Smail[3], Jack E. Birkin[3], Chian-Chou Chen[4], Scott C. Chapman[5], Ryley Hill[6], Claudia del P.Lagos[7,8,9], Cheng-Lin Liao[4,10], Elisabete da Cunha[8,11], Gabriela Calistro Rivera[12], Jianhang Chen[12], E. F. Jiménez-Andrade[13,14], Eric J. Murphy[14], Douglas Scott[6], A. M. Swinbank[3], Fabian Walter[15,16], R. J. Ivison[12,17], and Helmut Dannerbauer[18,19]
[1] Leiden Observatory, Leiden University, P.O. Box 9513, 2300 RA Leiden, The Netherlands; friascastillom@strw.leidenuniv.nl
[2] Faculty of Electrical Engineering, Mathematics and Computer Science, Delft University of Technology, Mekelweg 4, 2628 CD Delft, The Netherlands
[3] Centre for Extragalactic Astronomy, Department of Physics, Durham University, South Road, Durham DH1 3LE, UK
[4] Academia Sinica Institute of Astronomy and Astrophysics (ASIAA), No.1, Section 4, Roosevelt Road, Taipei 10617, Taiwan
[5] Department of Physics and Atmospheric Science, Dalhousie University, Halifax, Halifax, NS B3H 3J5, Canada
[6] Department of Physics and Astronomy, University of British Columbia, 6225 Agricultural Road, Vancouver V6T 1Z1, Canada
[7] International Centre for Radio Astronomy Research (ICRAR), M468, University of Western Australia, 35 Stirling Hwy, Crawley, WA 6009, Australia
[8] ARC Centre of Excellence for All Sky Astrophysics in 3 Dimensions (ASTRO 3D), Australia
[9] Cosmic Dawn Center (DAWN), Rådmandsgade 62, DK-2200 København, Denmark
[10] Graduate Institute of Astrophysics, National Taiwan University, Taipei 10617, Taiwan
[11] International Centre for Radio Astronomy Research, University of Western Australia, 35 Stirling Hwy, Crawley, WA 6009, Australia
[12] European Southern Observatory (ESO), Karl-Schwarzschild-Straße 2, D-85748 Garching bei München, Germany
[13] Instituto de Radioastronomía y Astrofísica, Universidad Nacional Autónoma de México, Antigua Carretera a Pátzcuaro # 8701, Ex-Hda. San José de la Huerta, Morelia, Michoacán, México C.P. 58089, México
[14] National Radio Astronomy Observatory, 520 Edgemont Road, Charlottesville, VA 22903, USA
[15] Max Planck Institute for Astronomy, Königstuhl 17, D-69117, Heidelberg, Germany
[16] National Radio Astronomy Observatory, Pete V. Domenici Array Science Center, P.O. Box O, Socorro, NM 87801, USA
[17] Institute for Astronomy, University of Edinburgh, Royal Observatory, Edinburgh EH9 3HJ, UK
[18] Instituto Astrofísica de Canarias (IAC), E-38205 La Laguna, Tenerife, Spain
[19] Dpto. Astrofísica, Universidad de la Laguna, E-38206 La Laguna, Tenerife, Spain
Received 2022 December 12; revised 2023 January 30; accepted 2023 February 1; published 2023 March 14

Abstract

We present the initial results of an ongoing survey with the Karl G. Jansky Very Large Array targeting the CO(J = 1–0) transition in a sample of 30 submillimeter-selected, dusty star-forming galaxies (SFGs) at $z = 2$–5 with existing mid-J CO detections from the Atacama Large Millimeter/submillimeter Array and NOrthern Extended Millimeter Array, of which 17 have been fully observed. We detect CO(1–0) emission in 11 targets, along with three tentative ($\sim 1.5\sigma$–2σ) detections; three galaxies are undetected. Our results yield total molecular gas masses of 6–23 $\times 10^{10}$ ($\alpha_{\rm CO}/1$) $M_{\odot}$, with gas mass fractions, $f_{\rm gas} = M_{\rm mol}/(M_{*}+M_{\rm mol})$, of 0.1–0.8 and a median depletion time of (140 ± 70) Myr. We find median CO excitation ratios of $r_{31} = 0.75 \pm 0.39$ and $r_{41} = 0.63 \pm 0.44$, with significant scatter. We find no significant correlation between the excitation ratio and a number of key parameters such as redshift, CO(1–0) line width, or $\Sigma_{\rm SFR}$. We only find a tentative positive correlation between r_{41} and the star-forming efficiency, but we are limited by our small sample size. Finally, we compare our results to predictions from the SHARK semi-analytical model, finding a good agreement between the molecular gas masses, depletion times, and gas fractions of our sources and their SHARK counterparts. Our results highlight the heterogeneous nature of the most massive SFGs at high redshift, and the importance of CO(1–0) observations to robustly constrain their total molecular gas content and interstellar medium properties.

Unified Astronomy Thesaurus concepts: High-redshift galaxies (734); Molecular gas (1073); Interstellar medium (847)

1. Introduction

Tracing the evolution of the molecular gas content in galaxies is necessary for a complete understanding of galaxy formation and evolution, as it provides the direct fuel for star formation (see reviews by Kennicutt & Evans 2012; Carilli & Walter 2013; Tacconi et al. 2020). The main component of the molecular gas, molecular hydrogen (H_2), cannot be excited in its rotation/vibration transitions in the low temperatures of the interstellar medium (ISM) of galaxies, due to the large separation between its energy levels ($\sim$500 K). Instead, ^{12}CO, the second most abundant molecule in galaxies after H_2, has been traditionally used to trace the kinematics, dynamics, and physical conditions of the cool gas in the ISM. The low upper-level temperature $T_{\rm ex}$ = 5.5 K and critical density of the rotational ground state ($J = 1-0$) of ^{12}CO, hereafter CO(1–0), means that this molecule is easily excited in a variety of galaxy environments, making it a useful tool for tracing the bulk of the cold molecular gas. The use of CO(1–0) only requires the assumption of a conversion factor, $\alpha_{\rm CO}$, to obtain the total cold molecular gas mass from the CO(1–0) luminosity (for a review, see Bolatto et al. 2013). Dust emission (Hildebrand 1983; Scoville et al. 2016; Liu et al. 2019; Wang et al. 2022) and the optically thin emission lines from neutral atomic carbon ([C I], Weiß et al. 2005; Walter et al. 2011; Valentino et al. 2018) are often used as alternative tracers of the molecular gas alongside CO.

Thanks to the improved capacities of (sub)millimeter interferometers, such as the Atacama Large Millimeter/submillimeter Array (ALMA), the Karl G. Jansky Very Large Array (VLA), and the NOrthern Extended Millimeter Array (NOEMA), studies of the redshifted CO emission have become common at high redshift (Carilli & Walter 2013; Hodge & da Cunha 2020). Blind CO line surveys, such as the VLA CO Luminosity Density at High Redshift (COLDz, Pavesi et al. 2018; Riechers et al. 2019) and the ALMA Spectroscopic Survey in the Hubble Ultra Deep Field (ASPECS; Walter et al. 2016; Decarli et al. 2019), have begun to unveil the CO excitation, molecular gas content and physical conditions of the ISM in star-forming galaxies (SFGs) at $z \sim 1$–6, establishing the most reliable evolution of the cosmic molecular gas density to date (Decarli et al. 2020; Riechers et al. 2020).

Obtaining direct observations of the CO(1–0) emission line at high redshift is a challenging task that requires long integration times, mostly due to the limitations of existing instrumentation in the current facilities in use. Therefore, studies commonly rely on the brighter mid- and high-J CO lines as alternative molecular gas tracers (e.g., Bothwell et al. 2013; Daddi et al. 2015; Yang et al. 2017; Boogaard et al. 2020; Birkin et al. 2021). This requires an assumption on the shape of the CO spectral line energy distribution (SLED) to infer the CO(1–0) luminosity. The CO excitation depends however on physical conditions and heating mechanisms at play in the cold ISM, and conversion factors span a wide range of values over the high-redshift galaxy population (Carilli & Walter 2013; Narayanan & Krumholz 2014; Sharon et al. 2016; Yang et al. 2017; Harrington et al. 2018; Boogaard et al. 2020; Riechers et al. 2020).

As noted, detecting CO(1–0) at high redshift requires several hours per source for even the brightest systems, the cold gas-rich submillimeter galaxies (SMGs; Casey et al. 2014; Hodge & da Cunha 2020). These dusty, high-infrared-luminosity ($L_{\rm IR} > 10^{12}$ $L_\odot$; Magnelli et al. 2012) systems have a peak cosmic volume density around $z \sim 2$–3 (Chapman et al. 2005; Danielson et al. 2017; Dudzeviciute et al. 2020). They are some of the most active star-forming systems in the universe, with star formation rates (SFRs) in the range of 100–1000 $M_\odot$ yr^{-1} (Magnelli et al. 2012; Cunha et al. 2015; Dudzeviciute et al. 2020), fed by large molecular gas reservoirs of 10^{10}–10^{11} $M_\odot$ (Greve et al. 2005; Tacconi et al. 2008; Bothwell et al. 2013; Birkin et al. 2021), and the brighter systems tend to be located at higher redshifts (Chen et al. 2022). Star formation in SMGs is typically distributed in dust structures with diameters of 2–3 kpc (Ikarashi et al. 2015; Simpson et al. 2015; Gullberg et al. 2019; Hodge et al. 2019). Such intense star-forming episodes are thought to be mainly triggered by mergers or interactions with neighboring galaxies. To date, CO(1–0) observations have been preferentially obtained toward bright, strongly lensed systems (e.g., Danielson et al. 2011; Thomson et al. 2012; Aravena et al. 2013; Harrington et al. 2018). Deriving the intrinsic CO(1–0) properties of lensed galaxies is however subject to uncertainties arising from lens modeling.

Our knowledge of the cold molecular gas content in non-lensed systems comes from targeted studies (Carilli et al. 2010; Riechers et al. 2011b, 2011a; Ivison et al. 2011; Sharon et al. 2016; Huynh et al. 2017; Kaasinen et al. 2019; Leung et al. 2019; Frias Castillo et al. 2022; Xiao et al. 2022). While valuable, carrying out a systematic study of a statistically significant sample of CO(1–0) emission of high-redshift galaxies has been hampered by the rather heterogeneous selection criteria applied in the different studies.

We have therefore undertaken a CO(1–0) survey of 30 unlensed, high-redshift ($z = 2$–5) submillimeter-selected SFGs with precise redshifts and existing moderate-J CO line detections from ALMA or NOEMA (Birkin et al. 2021; Chen et al. 2022; S. C. Chapman et al., in preparation). This survey more than doubles the existing number of unlensed $z > 2$ SFGs detected in CO(1–0). The paper is organized as follows: we review the sample selection and VLA observations in Section 2. In Section 3, we present the method used for extracting the integrated line fluxes. We then analyze the molecular gas mass content and excitation conditions of the sources in Section 4 and we present our conclusions in Section 5. Throughout this paper we assume a standard Lambda cold dark matter cosmology with $H_0 = 67.8$ km s^{-1} Mpc^{-1}, $\Omega_{\rm M} = 0.310$, and $\Omega_\Lambda = 0.690$ (Planck Collaboration et al. 2016).

2. Observations and Data Reduction

2.1. Sample

Our targets are selected from a sample of sources detected within 4 deg^2 of SCUBA-2 imaging of the UKIDSS Ultra Deep Survey (UDS), Cosmological Evolution Survey (COSMOS), Chandra Deep Field North (CDFN), and Extended Groth Strip (EGS) fields (Geach et al. 2017; Simpson et al. 2019). The brightest submillimeter sources in these fields were subsequently followed up with ALMA (AS2UDS, Stach et al. 2018; AS2COSMOS, Simpson et al. 2020) and SMA (EGS, CDFN, Hill et al. 2018) continuum imaging and further targeted with blind line scans using ALMA or NOEMA to obtain precise redshifts (Birkin et al. 2021; Chen et al. 2022; S. C. Chapman et al., in preparation). This provided initial constraints on the molecular gas content of a sample of 44 galaxies via mid-J CO transitions. From this parent sample, we selected sources at $z > 1.88$ to ensure the CO(1–0) line is redshifted into the VLA K and Ka bands. We excluded sources in the EGS field which only had a single transition detected and thus relied on photometric redshifts. Finally, we selected the 30 brightest sources based on mid-J CO and 850 μm flux densities ($S_{850} > 7.5$ mJy, Figure 1) with robust spectroscopic redshifts to follow up on CO(1–0) with the VLA. Because 850 μm flux density selects primarily on dust mass (e.g., Hayward et al. 2011; Liang et al. 2018), the brightness of these sources effectively provides a cold dust-mass-selected sample of high-redshift galaxies (Dudzeviciute et al. 2020). We currently do not have constraints on the presence of active galactic nuclei (AGN) within our sample. However, studies have found that around 15% of field SMGs host AGN (Wang et al. 2013), so we would expect 4−5 of our targets to have AGN activity. The final sample spans a range of redshift ($z = 2$–5) and dust mass ($M_{\rm d} = 1$–10×10^9 $M_\odot$). Here, we present the initial results of the survey, analyzing the 17 out of 30 targets that have been thus far fully observed.

2.2. Observations

We observed the CO(1–0) emission (rest-frame frequency: $\nu_{\rm rest} = 115.2712$ GHz) in 17 galaxies from our sample at $z = 2.26$–4.42 (VLA program ID: 21A-254; PI: Hodge). The observations were carried out between 2021 March 28 and 2021 June 1 under good weather conditions in D array

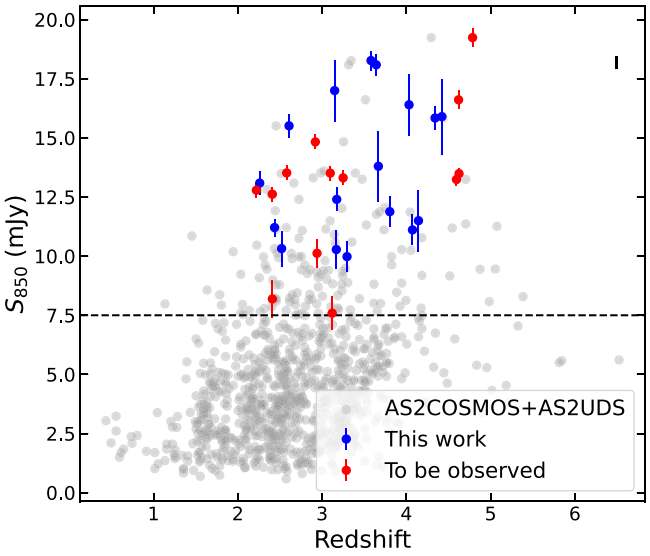

Figure 1. S_{850} flux density vs. redshift for the sources presented in this paper (blue-filled circles), with the parent samples from AS2COSMOS (Simpson et al. 2020) and AS2UDS (Stach et al. 2019; Dudzeviciute et al. 2020) shown as the gray dots. The sources still to be observed in our survey are shown as red dots. Given the time required to detect CO(1–0) in unlensed sources, we have targeted sources with $S_{850} > 7.5$ mJy. The majority of the parent sample only have photometric redshifts, so we further constrained the sample to those targets with spectroscopic redshifts of $z > 1.88$ from at least one CO spectral line (Birkin et al. 2021; Chen et al. 2022). The final sample spans a redshift range of $z = 2$–5 and a dust-mass range of 1–10 $\times$ 10^9 $M_\odot$.

configuration, in either one 4 hr or two 2 hr scheduling blocks per source. We used the *K*- or *Ka*-band receivers in combination with the WIDAR correlator configured to 8-bit sampling mode to observe a contiguous bandwidth of 2 GHz (dual polarization) at 2MHz spectral resolution. The largest angular scale of detectable emission is 7.″9 and 5.″3 for the *K* and *Ka* bands, respectively. Nearby quasars J1024-0052, J0215-022, J1419+5423, and J1400+6210 were observed for complex gain and pointing calibration. For bandpass and flux calibration, one of the quasars 3C286 and 3C48 was observed once per scheduling block (see Table 1 for details of individual sources). One of the sources, AS2COS0013.1, already had suitable archival VLA CO(1–0) observations carried out on 2017 March 10 in D-configuration (VLA program ID:17A-251; PI: Walter). The data were downloaded from the VLA archive, and after visually inspecting the data, some additional antennas were flagged.

The data were manually processed using `CASA` 6.4.3 (McMullin et al. 2007). Time ranges with poor visibilities were manually flagged. The calibrated visibilities were imaged using the `tclean` algorithm in `CASA`. We adopt natural weighting to maximize the signal-to-noise ratio (S/N) of the detections, which resulted in final beam sizes ranging from 2.″9 to 4.″7 at FWHM. The resulting data cubes reach a noise level of 41–98 μJy beam^{-1} for channels of 100 km s^{-1} width (see Table 1). The cubes are not continuum subtracted, but we do not detect any continuum emission down to a 2σ sensitivity threshold.

3. Results

3.1. Line Detections

To search for CO(1–0) emission, we initially create intensity-averaged 0th-moment maps by collapsing the cleaned data cubes over a velocity range corresponding to the FWHM of the respective mid-*J* CO line detection for each source, using the task `immoments` in CASA. We detect CO(1–0) toward 11 out of 17 targets at or above the 2σ significance level and tentatively detect another three at $\sim 1.5\sigma$ (Figure 2). We do not detect CO(1–0) emission toward AS2COS0009.1, AS2UDS014.0, or AEG3 (see Figure 14 in Appendix B). Using the 0th-moment maps, we check for any spatial offsets between the $J = 1$–0 and mid-*J* CO line emission for the detected sources. This is required for five sources, which show an offset of 0.″6, not significant given our resolution (2.″9–4.″7). Nevertheless, we extract the spectra from the CO(1–0) position for these sources.

We extract the spectra in an aperture of 5″ diameter to maximize the S/N and fit them using a single Gaussian model. Figure 3 shows the CO(1–0) line widths against the mid-*J* CO line widths. Previous studies have suggested that some high-redshift SMGs have line widths in CO(1–0) that are larger than those of the higher-*J* CO transitions (Ivison et al. 2010; Riechers et al. 2011b). Together with the fact that radiative transfer models underpredict the observed low-*J* CO emission, this suggests the presence of extended, low-excitation gas reservoirs in some SMGs (although not all, e.g., Hodge et al. 2012; Frias Castillo et al. 2022). We find that the widths of the lines agree with their mid-*J* counterparts within 2σ, with a median ratio $\mathrm{FWHM}_{\mathrm{CO(1-0)}}/\mathrm{FWHM}_{\mathrm{CO(J_{up},J_{up}-1)}} = 1.1 \pm 0.1$. Nevertheless, we have to caution that it is possible that there is fainter emission in the wings of the CO(1–0) lines that is currently not detected due to our sensitivity limitations. Given the sensitivity per channel of our data, and to avoid biasing our analysis, we choose to use the mid-*J* CO line widths to collapse the data cubes and obtain line fluxes. The integrated line fluxes are consistent within the uncertainties, regardless of whether we use the CO(1–0) or mid-*J* CO line widths.

To remove any bias due to line structure, we derive line fluxes using the intensity-weighted moments collapsed over a velocity range twice the corresponding mid-*J* CO line width for each source (Bothwell et al. 2013; Birkin et al. 2021):

$$M_0 = I_{\mathrm{CO}} = \int I_\nu d\nu. \quad (1)$$

We perform a curve-of-growth analysis on the 0th-moment maps to determine the optimal aperture to extract the line fluxes. In order to increase the S/N, we use the 0th-moment maps collapsed over the velocity range of one full line width ($\pm 0.5\times$ FWHM) of the respective mid-*J* CO line for each source. We then extract flux densities from a set of circular apertures of increasing diameter, from 1.″5 to 40″, and determine the point at which the flux converges. In Figure 13 in Appendix A, we show the curves of growth for all the sources as well as for their respective complex gain calibrators. Some of the fainter sources appear not to converge. This is due to the large-scale noise structures, more prominent due to the low S/N of the detections, which has also been observed in other data (Novak et al. 2020; Chen et al. 2022). We note that many of the brighter sources appear to be resolved compared to the phase calibrators, and show extended emission on roughly 6″ radius scales. Given the modest S/Ns of the detections, we choose to extract the flux from an aperture 2.″5 in radius for the sources with S/N < 3 (integrated over the FWHM of the CO(1–0) line), and then correct to the total flux using a factor of 1.8, as derived from the median curve of growth (following Chen et al. 2022). For sources with integrated S/N > 3, we extract

Table 1
Target Sample and Details of JVLA Observations

Target	R.A. J2000 (hh:mm:ss.ss)	Dec. J2000 (deg:mm:ss.ss)	z[a]	Date yyyy-mm-dd	rms Channel^{-1} [b] (μJy beam^{-1})	Beam (maj × min, P.A.)	Phase Calibrator	Flux Calibrator
AS2COS0008.1	10:02:49.2	+02:32:55.5	3.581	2021-05-18	87	4.″6 × 3.″0,38°	J1024-0052	3C286
				2021-05-18				
AS2COS0009.1	10:00:28.7	+02:32:03.6	2.260	2021-05-17	92	2.″9 × 2.″2,27°	J1024-0052	3C286
				2021-05-26				
AS2COS0013.1	10:00:35.3	+02:43:53.0	2.608	2017-03-10	76	3.″2 × 2.″3,−39°	J1041+0610	3C286
AS2COS0023.1	09:59:42.9	+02:29:38.2	4.341	2021-05-11	63	4.″4 × 3.″2,−6°	J1024-0052	3C286
AS2COS0031.1	09:59:23.0	+02:51:37.5	3.643	2021-04-20	58	4.″5 × 2.″8,13°	J1024-0052	3C286
AS2COS0054.1	09:58:45.9	+02:43:29.3	3.174	2021-04-04	86	3.″8 × 2.″5,8°	J1024-0052	3C286
AS2UDS010.0	02:15:55.9	−4:55:08.6	3.169	2021-05-21	98	4.″7 × 2.″6,−42°	J0215-0222	3C48
				2021-05-30				
AS2UDS011.0	02:16:30.8	−5:24:03.3	4.073	2021-04-17	84	4.″9 × 3.″0,−12°	J0215-0222	3C48
AS2UDS012.0	02:18:03.6	−4:55:27.2	2.520	2021-05-25	65	3.″5 × 2.″4,−37°	J0215-0222	3C48
AS2UDS014.0	02:17:44.3	−5:20:08.6	3.804	2021-05-04	81	4.″7 × 3.″0,−11°	J0215-0222	3C48
AS2UDS026.0	02:19:02.1	−5:28:56.9	3.296	2021-05-18	88	3.″8 × 2.″6,−16°	J0215-0222	3C48
AS2UDS126.0	02:15:46.7	−5:18:49.2	2.436	2021-05-22	92	4.″4 × 2.″1,−45°	J0215-0222	3C48
				2021-05-29				
AEG2	14:15:57.5	+52:07:12.4	3.668	2021-04-01	56	3.″2 × 2.″7,29°	J1419+5423	3C286
AEG3	14:15:47.1	+52:13:48.4	4.032	2021-04-02	41	4.″2 × 2.″9,17°	J1419+5423	3C286
CDFN1	12:35:55.9	+62:22:39.2	3.159	2021-03-29	90	2.″9 × 2.″5,39°	J1400+6210	3C286
CDFN2	12:35:51.5	+62:21:47.4	4.422	2021-03-31	63	4.″3 × 3.″5,0°	J1400+6210	3C286
CDFN8	12:36:27.2	+62:06:05.8	4.144	2021-03-28	75	3.″7 × 2.″9,4°	J1400+6210	3C286

Notes.
[a] Obtained from mid-J CO line detections.
[b] For 100 km s^{-1} channels.

the flux directly from an aperture 6″ in radius. The integrated fluxes, line widths, and line luminosities are summarized in Table 2. The 0th-moment maps and spectra of the detection and tentative detections are shown in Figure 2. The non-detections are shown in Appendix B.

We note that 6″ correspond to radii of ∼50 kpc at the median redshift of the sample. Studies of CO(1–0) on a handful of targeted sources have revealed the presence of extended cold gas reservoirs with sizes on the order of a few tens of kiloparsecs (Ivison et al. 2011; Emonts et al. 2016; Dannerbauer et al. 2017; Frayer et al. 2018). We currently lack the sensitivity and resolution to determine whether all the emission belongs to the same galaxy or if, for example, there could be companions that are contributing to the observed flux. Higher-resolution follow-up is necessary to derive robust sizes and establish the true extent of the gas reservoirs.

Finally, we also note that detectability of molecular gas emission is systematically affected by the increase in the temperature of the cosmic microwave background (CMB) with redshift ($T_{\rm CMB} = T_0(1+z)$). As da Cunha et al. (2013) showed, these effects become non-negligible when the CMB temperature becomes close to the gas temperature, $T_{\rm kin}$. However, Jarugula et al. (2021) and Harrington et al. (2021) have recently reported high kinetic temperatures ($T_{\rm dust} \sim 45$ K, $T_{\rm kin}/T_{\rm dust} \approx 2.5$) for strongly lensed dusty SFGs at high redshift, which might suggest that the CMB has a relatively minor effect on the suppression of the observed CO(1–0) luminosity (less than 15%). Further, we might expect to see a trend in excitation ratio with redshift if the CO(1–0) line was being heavily affected by CMB suppression. However, as we see in Section 4, there is no such trend. Detailed modeling of the CO SLED of each source would be necessary to derive accurate $T_{\rm kin}$ and therefore correct both the observed CO(1–0) and mid-J CO line fluxes.

3.2. Spectral Energy Distribution Fitting

In order to consistently derive key parameters such as SFRs and stellar masses for all our sources, we fit their spectral energy distributions (SEDs) with the high-redshift version of MAGPHYS (Cunha et al. 2015; Battisti et al. 2019), fixing the redshift as that corresponding to the mid-J CO transition, as they are higher S/N than our CO(1–0) data. For details of the photometry used, we refer the reader to Simpson et al. (2020) for sources in AS2COSMOS and Dudzeviciute et al. (2020) for AS2UDS.

For the five sources in the EGS and GOODS-North fields, AEG2, AEG3, CDFN1, CDFN2, and CDFN8, we compiled the available photometry. AEG2 has a counterpart in the DEEP2 Galaxy Redshift Survey photometric catalogs, and we use the published CFHT BRI measurements. For CDFN8, we obtain *Ks* and IRAC Bands 1 and 2 photometry from Wang et al. (2010) and Ashby et al. (2015). At long wavelengths, we use data from the GOODS-Herschel program of Elbaz et al. (2011) and the HerMES program of Oliver et al. (2012) to measure SPIRE 250, 350, and 500μm fluxes for sources in the CDFN and EGS fields, respectively. Finally, we use the SMA 870 μm flux density measurements from S. C. Chapman et al. (in preparation).

CDFN1 and CDFN2 are close to bright foreground sources, and we could not deblend the optical and infrared photometry to obtain stellar masses. Instead, we calculate the total infrared luminosities (8–1000 μm) by fitting a modified blackbody model to the Herschel and ALMA data, and convert to SFR following Kennicutt (1998) (correcting for a Chabrier initial mass function (IMF)). To check that the SFR values obtained through FIR SED modeling were consistent with those derived from MAGPHYS, we refit the far-IR (FIR) SED of the AS2COSMOS and AS2UDS sources and calculated their SFRs

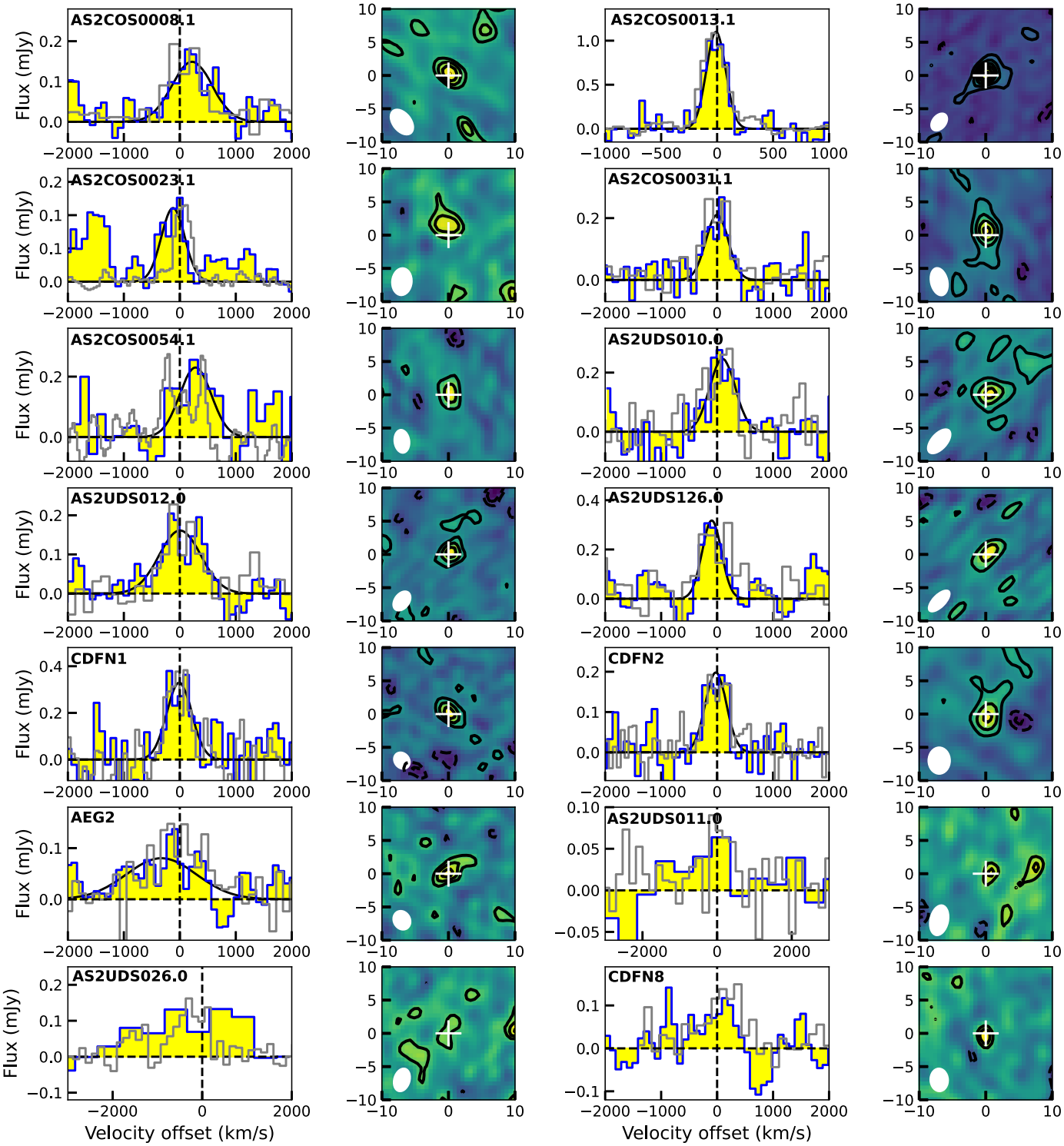

Figure 2. CO(1–0) line emission for the detections and three tentative detections in our sample of SMGs. The spectra (blue line and yellow fill, left panels) are extracted within a 2.″5 radius aperture to maximize the S/N. The spectra were fit with a single Gaussian model allowing for a varying line width, shown by the black curve. The 0th-moment maps (right panels) were collapsed over a velocity range equal to the FWHM of the respective mid-*J* CO emission line and show a $20'' \times 20''$ field of view. The systemic velocity is based on the redshift derived from the mid-*J* CO lines, and the gray histograms show the mid-*J* CO emission line, scaled down in flux density. The white cross indicates the peak of the mid-*J* CO line emission. Contours start at 2σ and increase in steps of 2σ, except for AS2COS0023.1, CDFN8, and AEG2, where they increase in steps of 1σ, and AS2COS0013.1, with steps of 3σ. The white ellipse shows the FWHM of the beam for each source.

from the inferred total infrared luminosities. The median ratio between the MAGPHYS- and FIR-derived SFRs is 1.10.2. We therefore consider the MAGPHYS and FIR-derived SFRs to be consistent. We adopt the median stellar mass of our sample for these two sources. Finally, AEG3 is also blended with a foreground source, which is further contaminating IRAC and

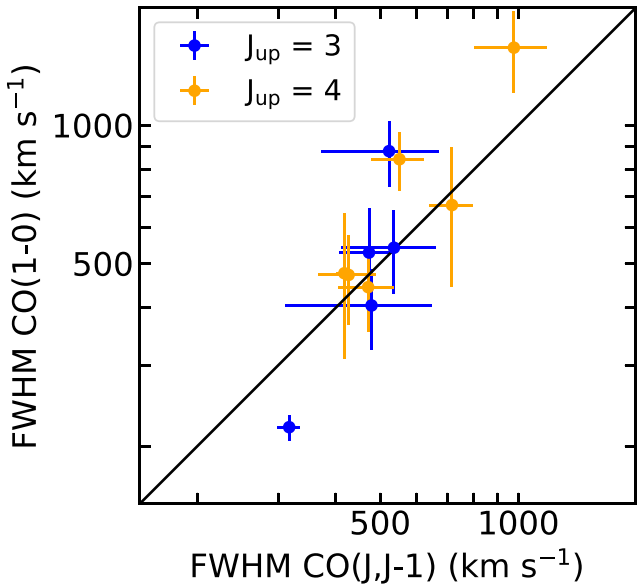

Figure 3. Comparison of the CO(1–0) and CO(3–2) or CO(4–3) line widths for our sample. The solid line shows the one-to-one relation. The line widths agree within 2σ for most of our sources, which suggests that, on average, there is not a significant amount of additional cool, diffuse gas being missed by the mid-J transitions.

Herschel fluxes, so we adopt both the median stellar mass and SFR from our sample for this source. Table 4 presents the final values used in this paper.

4. Analysis

In Section 3, we described our CO(1–0) observations and the homogenization of the SED modeling. We now turn toward the analysis of this data set. In Sections 4.1 and 4.2, we discuss the CO(1–0) luminosities and line widths in our sample, and infer the molecular gas mass fractions and depletion timescales. We then supplement our sample with literature data where available to study the *general* SMG population. Namely, we assess the reliability of dust-based mass estimates (Section 4.3) and the dependence of the CO excitation of the galaxy properties (Section 4.4). Finally, we compare our sample to the predictions from the SHARK semi-analytic models.

4.1. CO Line Luminosities

We convert CO line intensities into line luminosities following Solomon & Vanden Bout (2005):

$$L'_{\rm CO} = 3.25 \times 10^7\, I_{\rm CO}\, \nu_{\rm obs}^{-2}\, D_L^2\, (1+z)^{-3}\ {\rm K\ km\ s^{-1}\ pc^2}, \quad (2)$$

where $I_{\rm CO}$ is the integrated line flux from the 0th-moment map in Jy km s^{-1}, $\nu_{\rm obs}$ is the observed frequency in GHz and $D_{\rm L}$ is the luminosity distance in megaparsecs.

We find $L'_{\rm CO(1-0)}$ luminosities in the range of 7–17.5 $\times 10^{10}$ K km s^{-1} pc^2, with a median of $(10.2 \pm 2.1) \times 10^{10}$ K km s^{-1} pc^2 for the 14 sources. In Figure 4 (left), we show $L'_{\rm CO(1-0)}$ against redshift. Tentative detections are shown as open symbols, and non-detections are marked as 2σ upper limits. We see no variation with redshift, even after including all the non-lensed SMGs with CO(1–0) detections from the literature (Table 4). This stands in contrast with the positive trend for mid-J CO lines found by Birkin et al. (2021). However, since we are targeting the brightest 870 μm-selected sources from the AS2COSMOS, AS2UDS, CDFN, and EGS surveys, we are biased toward the most massive systems at their redshifts.

In Figure 4 (right) we show the line luminosities as a function of the CO(1–0) line widths. The $L'_{\rm CO}$–FWHM relation serves as a crude probe of the ratio between gas mass and dynamical mass (Harris et al. 2012; Bothwell et al. 2013). Our sources show no correlation between these two parameters, although we are limited by the narrow range in $L'_{\rm CO}$. For comparison, we include SMGs and SFGs from the literature with CO(1–0) detections (Table 4) and fit all the data with the model $\log_{10} L'_{\rm CO} = a\ \log_{10}({\rm FWHM}/{\rm FWHM_{med}}) + b$, where ${\rm FWHM_{med}}$ is the median FWHM of all the sources being considered for the fit, 550 km s^{-1}. The fit yields a significant slope $a = 1.6 \pm 0.3$ and $b = 10.8 \pm 0.1$, consistent with the values found from mid-J CO emission (Bothwell et al. 2013; Birkin et al. 2021).

4.2. Gas Masses, Gas Fractions, and Depletion Times

The CO(1–0) emission line is the most direct probe of total molecular gas mass. We calculate the total cold molecular gas mass from the CO(1–0) line luminosities using

$$M_{\rm mol} = 1.36 \alpha_{\rm CO} L'_{\rm CO}\ M_\odot, \quad (3)$$

where the 1.36 factor accounts for the helium abundance and $\alpha_{\rm CO}$ is the CO-H_2 conversion factor in units of $M_\odot$ (K km s^{-1} pc^2)$^{-1}$. This conversion factor depends on several physical parameters, such as temperature, cloud density, and metallicity (Narayanan et al. 2012; Bolatto et al. 2013). It is common to assume an ULIRG-like value of $\alpha_{\rm CO} \sim 1$ for starburst systems at high redshift, such as our SMGs. However, recent studies based on dynamical modeling point toward a value of $\alpha_{\rm CO} = 1$–2 (Danielson et al. 2011; Rivera et al. 2018; Birkin et al. 2021; Frias Castillo et al. 2022). Assuming $\alpha_{\rm CO} = 1$, we find a median $M_{\rm mol} = (1.4 \pm 0.3) \times 10^{11}\ M_\odot$. Compared to the average SMG population, which has a median of $(9.1 \pm 0.7) \times 10^{10}\ M_\odot$ (Birkin et al. 2021), our targets are almost a factor of 2 more gas-rich.

With the gas measurements, we can also explore two key parameters to understand the ISM properties of the galaxies in our sample, the gas fraction and depletion timescale, defined as

$$f_{\rm gas} = \frac{M_{\rm mol}}{M_{\rm mol} + M_*}, \quad (4)$$

$$t_{\rm dep} = \frac{M_{\rm mol}}{\rm SFR}, \quad (5)$$

which correspond, respectively, to the fraction of baryons available for star formation and the time that it would take for the systems to use their current gas supply given its current galaxy-integrated SFR, in the absence of feedback.

Figure 5 (left) shows the total molecular gas mass as a function of SFR. The dashed lines show the location of constant molecular gas depletion timescale. Our targets have a median of (140 ± 70) ($\alpha_{\rm CO}$) Myr, including tentative detections and upper limits. This is in agreement with $t_{\rm dep} = (210 \pm 40)$ Myr found from mid-J CO lines by Birkin et al. (2021), but significantly shorter than the $\sim$1 Gyr that would be expected from scaling relations (Tacconi et al. 2018)—although these have been claimed empirically only up to $z \sim 2.5$. In Figure 5 (right), we show the total molecular gas mass as a function of stellar mass, with the dashed lines showing the location of

Table 2
Summary of Line Observations

Target	[a]S_{870} (mJy)	$I_{CO(1-0)}$ (Jy km s^{-1})	FWHM $_{CO(1-0)}$ (km s^{-1})	S/N$_{peak}$	$L'_{CO(1-0)}$ ($\times10^{10}$) (K km s^{-1} pc^{-2})	SFR ($M_\odot$ yr^{-1})	M_* ($M_\odot$ ($\times10^{10}$))	f_{gas}	t_{dep} (Myr)
AS2COS0008.1	18.3 ± 0.4	0.21 ± 0.07	850 ± 120	2.6	11.6 ± 3.9	1400^{+100}_{-140}	51^{+12}_{-7}	0.23 ± 0.07	110 ± 40
AS2COS0009.1	13.1 ± 0.3	<0.14	⋯	0.2	<3.6	130^{+3}_{-0}	9^{+0}_{-1}	<0.4	<380
AS2COS0013.1	15.5 ± 0.4	0.34 ± 0.07	220 ± 14	8.8	11.0 ± 2.2	920^{+120}_{-130}	28^{+8}_{-7}	0.35 ± 0.08	160 ± 40
AS2COS0023.1	15.8 ± 0.3	0.09 ± 0.04	480 ± 170	2.1	7.0 ± 3.1	590^{+21}_{-13}	$6^{+0.1}_{-0.1}$	0.61 ± 0.10	160 ± 70
AS2COS0031.1	18.1 ± 0.4	0.22 ± 0.06	470 ± 100	3.6	12.7 ± 3.5	450^{+100}_{-140}	$5^{+0}_{-0.1}$	0.79 ± 0.05	390 ± 160
AS2COS0054.1	12.4 ± 0.2	0.23 ± 0.09	670 ± 220	2.7	10.2 ± 3.9	1000^{+120}_{-130}	9^{+4}_{-2}	0.60 ± 0.13	140 ± 50
AS2UDS010.0	10.3 ± 0.8	0.38 ± 0.10	540 ± 110	3.4	17.3 ± 4.7	570^{+90}_{-120}	35^{+18}_{-14}	0.40 ± 0.14	410 ± 140
AS2UDS011.0	11.1 ± 0.7	0.07 ± 0.04	⋯	1.3	4.7 ± 2.7	959^{+170}_{-190}	32^{+16}_{-13}	0.17 ± 0.36	67 ± 40
AS2UDS012.0	10.3 ± 0.7	0.36 ± 0.07	880 ± 140	3.7	11.1 ± 2.3	400^{+0}_{-5}	21^{+0}_{-1}	0.42 ± 0.05	380 ± 80
AS2UDS014.0	11.9 ± 0.6	<0.12	⋯	−0.2	<7.3	690^{+160}_{-40}	14^{+2}_{-2}	<0.4	<140
AS2UDS026.0	10.0 ± 0.6	0.13 ± 0.05	⋯	1.4	6.3 ± 2.9	350^{+80}_{-100}	28^{+12}_{-9}	0.23 ± 0.42	250 ± 120
AS2UDS126.0	11.2 ± 0.4	0.17 ± 0.10	400 ± 80	2.8	4.9 ± 2.9	690^{+340}_{-260}	69^{+93}_{-44}	0.09 ± 0.07	100 ± 80
AEG2	13.8 ± 1.5	0.12 ± 0.06	1500 ± 300	2.6	11.4 ± 3.4	580^{+10}_{-10}	$5^{+1.0}_{-0.1}$	0.77 ± 0.06	270 ± 80
AEG3	16.4 ± 1.3	<0.04	⋯	−0.1	<2.7	[b]690^{+270}_{-120}	[b]25^{+10}_{-20}	<0.1	<50
CDFN1	17.0 ± 1.3	0.39 ± 0.10	530 ± 130	4.1	17.5 ± 4.5	1150^{+30}_{-40}	[b]25^{+10}_{-16}	0.49 ± 012	210 ± 50
CDFN2	15.9 ± 1.6	0.17 ± 0.05	440 ± 90	3.1	12.9 ± 3.8	1700^{+80}_{-50}	[b]25^{+10}_{-16}	0.42 ± 0.12	100 ± 30
CDFN8	11.5 ± 1.3	0.10 ± 0.06	590 ± 210	1.8	7.0 ± 4.3	800^{+180}_{-120}	62^{+16}_{-18}	0.13 ± 0.13	120 ± 80
Median	13.1 ± 1.5	0.20 ± 0.04	530 ± 100		10.2 ± 2.1	690^{+270}_{-120}	25^{+10}_{-16}	0.35 ± 0.21	140 ± 70

Notes. The columns give the source name, 870 μm flux density, CO(1–0) integrated flux, CO(1–0) FWHM (from a single Gaussian fit to the spectra), peak S/N, CO(1–0) line luminosity, SFR, stellar mass, gas fraction, and depletion time. Non-detections are reported as 2σ upper limits.
[a] 870 μm flux density measurements obtained from ALMA for sources in the COSMOS and UDS fields (Stach et al. 2018; Simpson et al. 2020) and from the SMA for those in the CDFN and EGS fields (Hill et al. 2018).
[b] Reported values are the median of the whole sample.

constant gas fraction. We find gas fractions in the range of 10%–80%, with a median f_{gas} of 0.35 ± 0.21. We see a larger amount of scatter in gas fractions than in depletion timescales, driven by the wide range in stellar masses (0.6 dex).

We also show the evolution of the gas fraction and depletion timescale for our sources in Figure 6, color coded by their main sequence (MS) offset, where the MS is defined following Speagle et al. (2014). While there is no trend with MS offset for depletion time, the sources with the largest offset tend to have larger gas fractions, indicating a larger availability of molecular gas to feed the ongoing starburst. Both of these parameters have been shown to follow scaling relations with redshift from previous studies of SFGs (e.g., Genzel et al. 2015; Tacconi et al. 2018; Liu et al. 2019; Tacconi et al. 2020), shown in Figure 6 as solid and dashed lines for sources on and above the MS, respectively. Due to the small sample size and large scatter, even after including values from our literature compilation, we refrain from fitting the data. We do not see evolution of t_{dep} or f_{gas} with redshift for the massive, gas-rich SMGs that comprise our sample. Our gas fractions and depletion times are below the values predicted by the scaling relations for the median stellar mass of our sample. This is partly because Tacconi et al. (2018) use a Milky Way value for α_{CO} of 4.36 $M_\odot$ (K km s^{-1} pc^2)$^{-1}$. Furthermore, the relations were derived from mid-J CO transitions and used excitation correction factors of r_{31} and r_{41} of 0.42 and 0.31, respectively, to obtain total molecular gas masses. These values are lower than the median for our sources (Section 4.4), which results in an overestimation of the total molecular gas mass, and therefore higher gas fractions and depletion times. If we modify the scaling relations to $\alpha_{CO} = 1$ (gray lines in Figure 6), we find a better agreement with the expected depletion times.

4.3. Comparison with Dust-based Gas Mass Estimates

The Rayleigh–Jeans (RJ) tail of dust emission is almost always optically thin, which means it can be used as a tracer of the total dust mass and therefore the molecular gas mass, provided that the dust emissivity per unit mass and the dust-to-gas abundance ratio can be constrained. Under the assumption of a mass-weighted cold dust temperature $T_{dust} = 25$ K (which is claimed to be a representative value for both local SFGs and high-redshift galaxies) and a dust emissivity index $\beta = 1.8$, the CO(1–0) luminosity and 850 μm continuum flux have been shown to correlate for a range of galaxy populations (e.g., Scoville et al. 2016 for local SFGs, ULIRGs, and high-redshift SMGs, and Kaasinen et al. 2019 for $z \sim 2$ SFGs).

Using the 870 μm flux density measurements for our sources, we can estimate the rest frame L_ν(850 μm) and therefore M_{mol} values following Scoville et al. (2016):

$$M_{mol} = 1.78 S_{\nu_{obs}} (1+z)^{-4.8} \times \left(\frac{\nu_{850}}{\nu_{obs}}\right)^{3.8} D_L^2 \left(\frac{6.7 \times 10^{19}}{\alpha_{850}}\right) \frac{\Gamma_0}{\Gamma_{RJ}} \, 10^{10} M_\odot, \quad (6)$$

where $\nu_{obs} = 345$ GHz, ν_{850} is the rest-frame frequency used to calibrate α_{850}, D_L is in gigaparsecs and α_{850} is the conversion factor between L_{870} and molecular gas mass. Γ_{RJ} is the correction for departures in the rest frame of the Planck function from the RJ tail, with $\Gamma_0(z = 0, T_d = 25K) = 0.71$. We note that this method was calibrated using $\alpha_{CO} = 6.5$ $M_\odot$ (K km s^{-1} pc^2)$^{-1}$, whereas we use $\alpha_{CO} = 1$ for our sample. Therefore, for a consistent comparison with CO(1–0), we

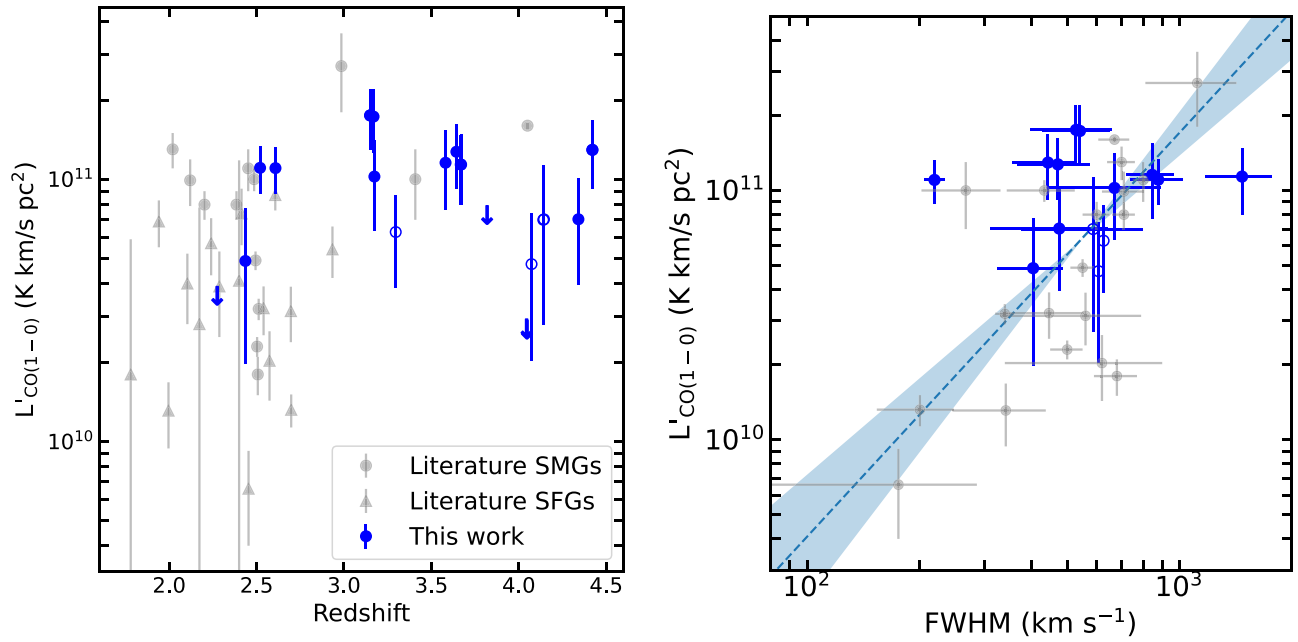

Figure 4. Left: integrated CO(1–0) line luminosities for our sample as a function of redshift. Open circles indicate tentative (2σ) detections and upper limits are marked as downward arrows. We show all non-lensed SMGs with CO(1–0) detections from the literature for comparison, as well as $z = 2$ SFGs from Kaasinen et al. (2019) and Boogaard et al. (2020). We find no evidence of evolution of $L'_{\rm CO(1-0)}$ with redshift. Right: Integrated CO(1–0) line luminosities as a function of CO(1–0) line width. We fit all the data (including literature values) with the model $\log_{10}L'_{\rm CO} = a\ \log_{10}({\rm FWHM}/{\rm FWHM_{med}}) + b$, where $\rm FWHM_{med}$ is the median FWHM of all the sources being considered for the fit, 550 km s^{-1}. The fit yields a slope $a = 1.6 \pm 0.3$ and $b = 10.8 \pm 0.1$.

divide the values obtained from the dust continuum by 6.5 to obtain total molecular gas masses.

Figure 7 shows the dust-based gas masses compared with the CO(1–0) gas masses. Since our sample probes a relatively narrow range in S_{850}, we expand the range by comparing with $z \sim 2$ SFGs from Kaasinen et al. (2019) and the VLASPECS SFGs from Boogaard et al. (2020) and Riechers et al. (2020). To test whether there is a correlation between the total molecular gas masses derived from CO(1–0) and 870 μm continuum, we calculate the Pearson's (τ) and Spearman's (ρ) correlation coefficients. These coefficients measure the strength and direction of a linear and monotonic association (so we do not have to assume the underlying shape of the relation), respectively, between two variables. The coefficients can take values between $+1$ (perfect positive association) and -1 (perfect negative association), with 0 being no correlation. Assuming a null hypothesis of no correlation, the p-value represents the probability that the strength of the observed correlation is due to chance. We find $\tau = 0.1$ (p-value $= 0.7$) and $\rho = 0.2$ (p-value $= 0.5$) when considering just the values for our sample, meaning that the gas masses for our targets as traced by the two tracers do not appear to be correlated. We note however that we are limited by the small sample size. After including the VLASPECS (Riechers et al. 2020) and $z = 2$ SFGs from Kaasinen et al. (2019), we find $\tau = 0.9$ (p-value $= 4 \times 10^{-8}$) and $\rho = 0.8$ (p-value $= 3 \times 10^{-7}$), showing a strong positive linear correlation between the two variables.

We note that, at these redshifts, our continuum flux density measurements probe rest-frame wavelengths of $\sim$250 μm, where the SED deviates significantly from the RJ tail of the dust emission. As a result, the 850 μm continuum–based gas masses have considerable uncertainties. Nevertheless, they agree with the CO(1–0)–based gas masses to about a factor of 2. However, caution is needed to draw strong conclusions from these results.

4.4. CO Spectral Line Energy Distributions and Line Ratios

The study of the CO excitation in galaxies provides key insights into the properties and state of their ISM, such as gas density and heating mechanisms. In Figure 8 we show the CO SLEDs for our sample normalized to the CO(1–0) transition. Because of the way our sample was constructed, each galaxy is only detected in either CO(3–2) or CO(4–3), which prevents modeling of the CO SLED for individual sources. However, we plot the statistical CO SLEDs derived by Birkin et al. (2021) for $z = 1.2$–4.8 SMGs and by Boogaard et al. (2020) for $z = 2.5$ SFGs, as well as for the *cosmic eyelash* (Danielson et al. 2011) for comparison. The non-detected sources, AS2COS0009.1, AS2UDS014.0, and AEG3, show super-thermal excitation, as their CO(3–2) or CO(4–3) luminosity is significantly higher than our 2σ upper limits on CO(1–0). All the other galaxies in our sample are consistent with thermal or subthermal excitation within the error bars. The $I_{\rm CO(3-2)}/I_{\rm CO(1-0)}$ excitation is also consistent with the Boogaard et al. (2020) and Birkin et al. (2021) statistical SLEDs, while $I_{\rm CO(4-3)}/I_{\rm CO(1-0)}$ appears to be slightly higher than reported in Birkin et al. (2021).

The ratios of CO line luminosities can be used as excitation indicators of the average state of the molecular gas, and are usually reported as

$$r_{J1} = \frac{L'_{\rm CO(J-(J-1))}}{L'_{\rm CO(1-0)}}. \quad (7)$$

We measure line luminosity ratios between the CO(3–2) and the CO(1–0) emission lines of 0.31–1.16, with a median of $r_{31} = 0.75 \pm 0.39$. For the CO(4–3) line, we find ratios in the range of 0.37–1.26, with a median $r_{41} = 0.63 \pm 0.44$, where the errors are calculated as the median absolute deviation. These ratios, listed in Table 3, reveal a large spread in the excitation conditions from galaxy to galaxy, from low excitation ($r_{31} \sim$

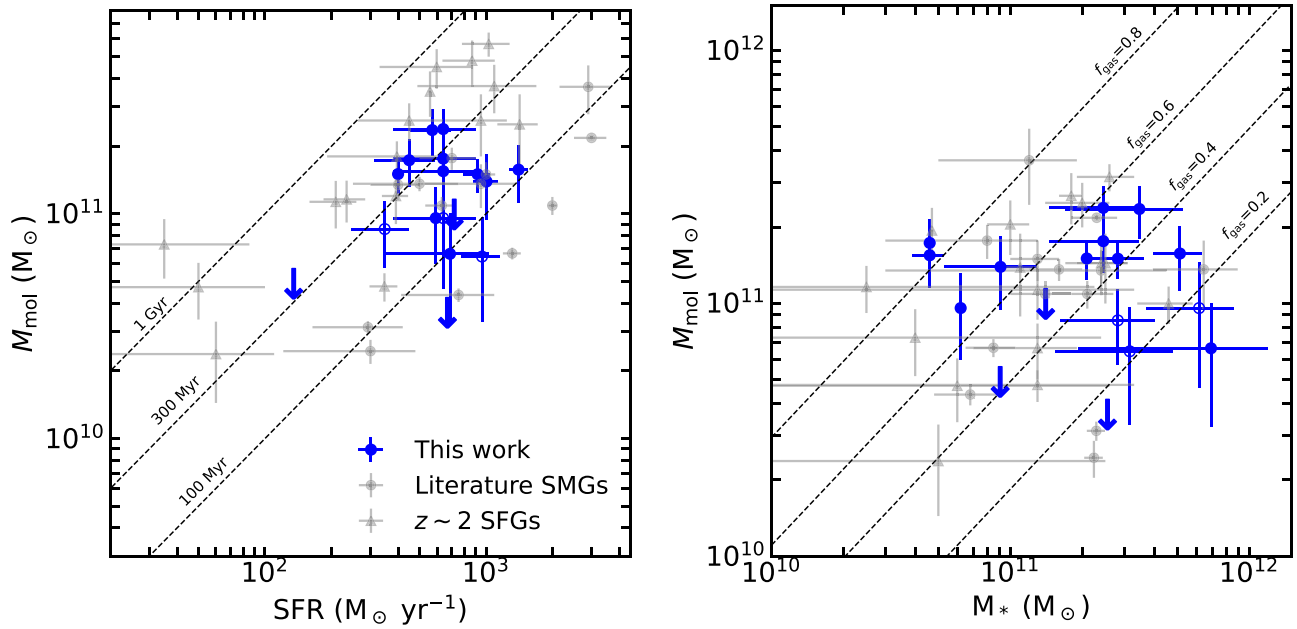

Figure 5. Left: M_{mol} vs. SFR for our sources, compared to unlensed SMGs with CO(1–0) measurements from the literature, as well as $z\sim2$ SFGs from Kaasinen et al. (2019) and Riechers et al. (2020). The gas masses from the literature compilation have been adjusted to $\alpha_{CO}=1$. The dashed lines show the location of constant gas depletion timescales. Our targets have a median of (140 ± 70) (α_{CO}) Myr, in agreement with $t_{dep}=(210\pm40)$ Myr found from mid-J CO lines for the latest SMG compilations in Birkin et al. (2021). Right: same, but in the M_{mol}-M_* plane. Dashed lines show the location of constant gas fraction. We find gas fractions in the range of 10%–80%, with a median f_{gas} of 0.35 ± 0.21 and a scatter of 0.6 dex.

0.3) to super-unity ratios ($r_{31}\sim$ 1.2, $r_{41}\sim1.5$). Under normal conditions in SMGs, the ISM is dominated by cold molecular gas and the CO emission is optically thick, leading to $r_{J1}\leqslant1$. The superthermal CO excitation can occur if (a) the CO emission is optically thin, (b) CO(1–0) is self-absorbed, (c) emission is coming from ensembles of small, unresolved, optically thick clouds, or (d) the emission is optically thick and has temperature gradients (Bolatto et al. 2000, 2003). It is also possible that, due to the low S/N of our detections, we are missing low surface brightness CO(1–0) emission below our detection threshold.

The median r_{31} value is comparable to that of other high-redshift galaxies reported in the literature. In the VLASPECS survey (Riechers et al. 2020), the median r_{31} for MS galaxies at $z=2$–3 is 0.84 ± 0.26; Xiao et al. (2022) reported an r_{31} of 0.8 for two starburst galaxies in a $z=2.5$ protocluster, and Sharon et al. (2016) found $r_{31}=0.78\pm0.27$ for a sample of lensed and unlensed SMGs at $z\sim2$. Our value for r_{31} is higher than the ratio found by Ivison et al. (2011), 0.55 ± 0.05, for SMGs at $z=2.2$–2.5, and consistent with 0.63 ± 0.12 from Birkin et al. (2021). There are fewer data points available on r_{41}: our $r_{41}=0.63\pm0.11$ is consistent with $r_{41}=0.56\pm0.20$ and 0.45 ± 0.12, found, respectively, for the unlensed SMGs J13120+4242 and GN20 (Carilli et al. 2010; Frias Castillo et al. 2022).

We now look for correlations between the molecular gas excitation and other observed and derived quantities. The 870 μm flux density is derived from ALMA measurements (Stach et al. 2019; Simpson et al. 2020, S. C. Chapman et al., in preparation), and we calculate the MS offset following Speagle et al. (2014). Although recent studies found evidence for a flattening of the MS at the high-stellar-mass end (Whitaker et al. 2014; Schreiber et al. 2015; Leslie et al. 2020), this is mostly seen at $z<1.5$. At high redshift, a linear model is still preferred by the available data (Lee et al. 2018; Leslie et al. 2020). SFR and stellar masses are obtained through SED fitting as described in Section 3. We calculate the Spearman's and Pearson's rank correlation coefficients for both ratios separately (including the literature compilation) and find no significant trends with redshift, CO(1–0) FWHM, SFR (Figure 9), SFR surface density (Figure 10), 870 μm flux density, and MS offset (not pictured).

A previous study by Sharon et al. (2016) found a positive trend between star formation efficiency (SFE = SFR/M_{mol}) and CO excitation in a sample of SMGs and AGN at $z\sim2$–3. Similar trends have also been found in the local universe, in ULIRGs (Papadopoulos et al. 2012; Greve et al. 2014) and IR-luminous galaxies (Yao et al. 2003). We show our ratios as a function of SFE in Figure 10 (left). We calculate the Spearman's and Pearson's rank correlation coefficients for both ratios together and independently (assuming non-detections as lower limits), but do not find any significant correlation between line excitation and SFE.

The CO excitation has also been proposed to correlate with the SFR surface density, Σ_{SFR} (Narayanan & Krumholz 2014; Daddi et al. 2015; Boogaard et al. 2020; Valentino et al. 2020). Based on high-resolution ALMA imaging, the dust-emitting regions of our targets in the COSMOS and UDS fields have radii in the range of 0.7–2.4 kpc, with a median radius of 1.4 ± 0.5 kpc (Gullberg et al. 2019; Stach et al. 2019; Simpson et al. 2020; S. Ikarashi et al., in preparation). The SMA 850 μm imaging of the sources in the EGS and GOODS-North fields does not have the necessary resolution to derive dust continuum sizes, so we use the median size of the AS2COSMOS and AS2UDS sources, 1.4 ± 0.5 kpc. We calculate Σ_{SFR}, and plot it as a function of the flux ratios of CO(3–2) and CO(4–3) over CO(1–0) in Figure 10 (right). We note that the dust continuum traces star-forming regions, and is often found to be smaller than the extent of the CO(1–0)-traced cold molecular gas reservoirs (e.g., Simpson et al. 2015;

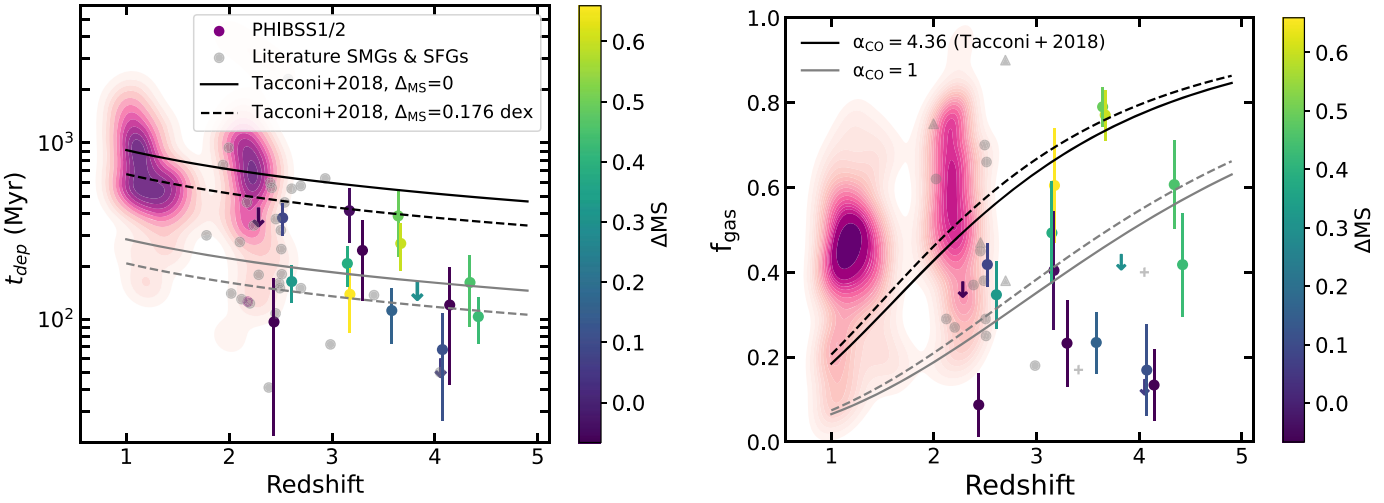

Figure 6. Depletion time (left) and gas fraction (right) as a function of redshift for our SMG sample, color coded by their offset from the MS. The solid and dashed lines show the scaling relations from Tacconi et al. (2018) for sources on the MS and ×1.5 above the MS, respectively, for a stellar mass of $2.5 \times 10^{11}\,M_{\odot}$, the median stellar mass of our sample. We do not see evidence of evolution with redshift for either parameter. Our gas fractions and depletion times are below the values predicted by the scaling relations, although this disagreement is reduced if we rescale the relations to $\alpha_{CO} = 1$ (gray lines).

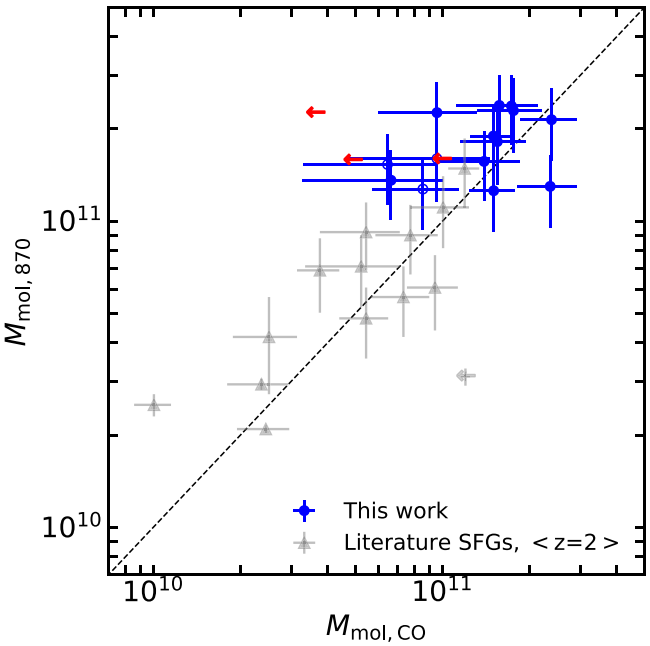

Figure 7. Comparison between the gas masses derived from CO(1–0) line luminosities and 870 μm continuum flux densities for our sample, as well as with $z = 2$ SFGs from Boogaard et al. (2020), Riechers et al. (2020) and Kaasinen et al. (2019) with CO(1–0) line detections. We convert the molecular gas masses of the SFGs to the same α_{CO} factor of 1 for an equal comparison with our sample. The gas masses agree within a factor of 2, although there is significant scatter around the 1:1 line shown by the dashed line.

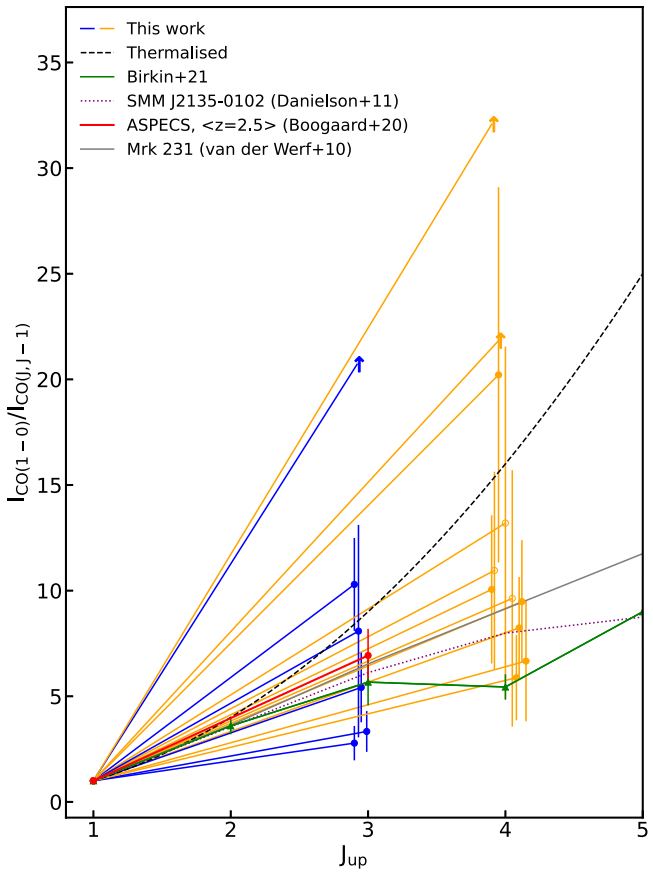

Figure 8. CO ladders for our targets normalized to the CO(1–0) integrated line flux. The targets show excitation that is, on average, comparable with the cosmic eyelash (Danielson et al. 2011) and the average SMGs at high redshift (Birkin et al. 2021), although there is a large scatter for both ratios. For comparison, we also show the average SLED for $z = 2.5$ SFGs from the VLASPECS survey (Boogaard et al. 2020; Riechers et al. 2020) and the QSO Mrk 231 (van der Werf et al. 2010). Data points are shifted on the x-axis for easier visualization.

Barro et al. 2016; Hodge et al. 2016; Dannerbauer et al. 2017; Rivera et al. 2018; Simpson et al. 2020).

To assess the correlation between the CO excitation and Σ_{SFR}, we again calculate the corresponding Spearman's and Pearson's rank correlation coefficients. For r_{31}, the tests find no significant correlation (Spearman's $\rho = -0.3$, $p = 0.6$, and Pearson's $\tau = 0.2$, $p = 0.7$). For r_{41}, the Spearman's test shows a strong positive correlation between the variables, $\rho = 0.8$, and a p-value of 0.023, meaning that we can reject the null hypothesis that the samples are uncorrelated, while Pearson's test finds a strong positive correlation ($\tau = 0.7$) but we cannot rule out the possibility of them being uncorrelated from the p-value of 0.1. Since we are limited by the small sample size and large error bars, we refrain from fitting the data. We compare

Table 3
CO Line Ratios

Target	r_{31}	r_{41}
AS2COS0008.1	⋯	0.63 ± 0.22
AS2COS0009.1	>0.97	⋯
AS2COS0013.1	1.16 ± 0.24	⋯
AS2COS0023.1	⋯	1.26 ± 0.56
AS2COS0031.1	⋯	0.51 ± 0.15
AS2COS0054.1	⋯	0.42 ± 0.18
AS2UDS010.0	0.60 ± 0.18	⋯
AS2UDS011.0*	⋯	1.46 ± 0.93
AS2UDS012.0	0.37 ± 0.11	⋯
AS2UDS014.0	⋯	>0.68
AS2UDS026.0*	⋯	1.22 ± 0.51
AS2UDS126.0	0.90 ± 0.56	
AEG2	⋯	0.61 ± 0.32
AEG3	⋯	>1.67
CDFN1	0.31 ± 0.09	⋯
CDFN2	⋯	0.59 ± 0.18
CDFN8	⋯	1.07 ± 0.38
Median	0.75 ± 0.39	0.63 ± 0.44

these to the line excitation predictions from Narayanan & Krumholz (2014) for unresolved observations of CO transitions, shown by the dashed lines for the two ratios r_{31} and r_{41} in blue and orange, respectively. While the ratios qualitatively agree with the theoretical models, observations show a large amount of scatter.

4.5. Comparison with Semi-analytic Models

How do our measurements of molecular gas mass in bright SMGs compare to current theoretical models? Due to their $M_\star$ and SFR, SMGs pose a challenge to galaxy evolution simulations. Recently, state-of-the-art hydrodynamical simulations such as EAGLE, SIMBA, and IllustrisTNG have been able to reproduce some key aspects of the SMG population, albeit using very different assumptions. However, due to their limited simulation volumes, they do not contain enough sources with $S_{850} \geqslant 10$ mJy, whereas our sample spans $S_{850} \approx 10$–20 mJy.

We have chosen to compare our data to predictions from the SHARK semi-analytical model (Lagos et al. 2018) applied to the SURFS N-body simulation (Elahi et al. 2018). SHARK has been able to reproduce SMG number counts and redshift distribution without having to introduce, e.g., top-heavy stellar initial mass function (Lagos et al. 2020). We adopt the broadband continuum fluxes predicted using the Lagos et al. (2019) framework. Thanks to the large box size of the SURFS simulation ($210^3\,(\mathrm{cMpc}/h)^3$), SHARK includes a sizeable population of $S_{850} \geqslant 10$ mJy SMGs which can be directly compared to our sample. Such bright SMGs are mostly absent from the recent hydrodynamical simulations such as EAGLE (Schaye et al. 2015; McAlpine et al. 2019) or SIMBA (Dave et al. 2019; Lovell et al. 2021), as these have volumes $\approx 10\times$ smaller.

For comparison, we select galaxies from the SHARK catalog spanning $z = 2$–5. We compare four key parameters: S_{850}, molecular gas mass $M_{\rm mol}$, $M_\star$, and SFR. As shown in Figure 11, SHARK galaxies with $S_{850} \geqslant 10$ mJy have molecular gas masses consistent with our measurements. At higher 850 μm fluxes, the observed $M_{\rm mol}$ values tend to fall on the

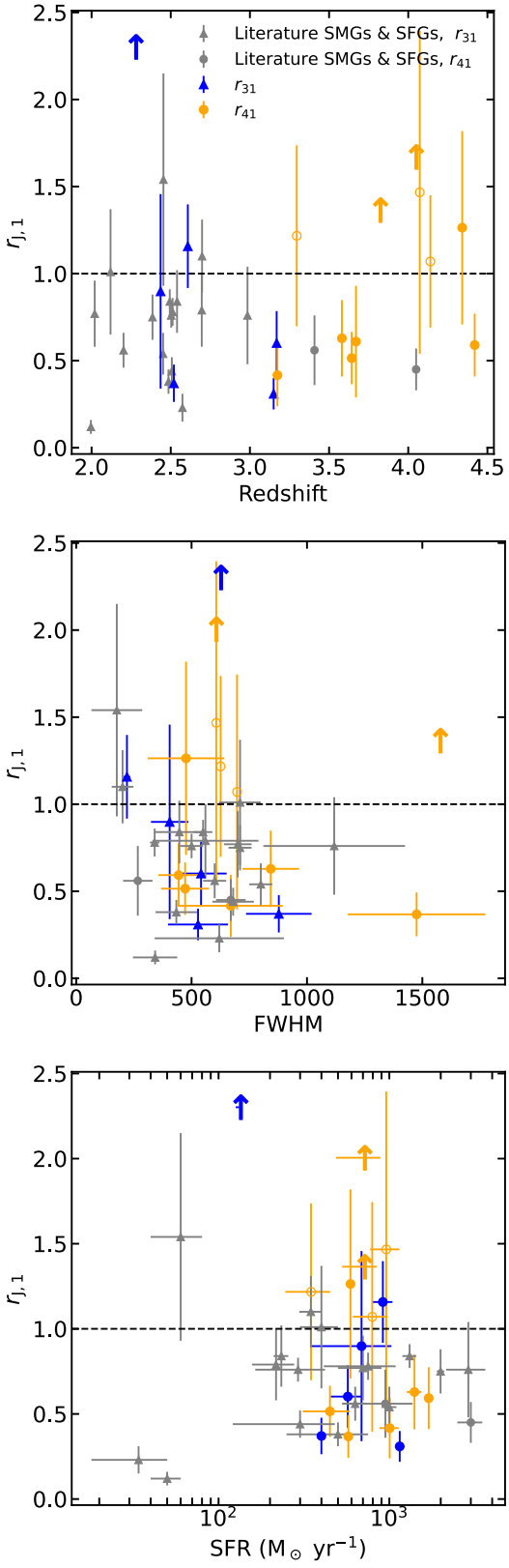

Figure 9. CO(3–2)/CO(1–0) (blue) and CO(4–3)/CO(1–0) (orange) excitation ratios as a function of redshift (top), CO(1–0) line width (middle) and SFR (bottom). Tentative detections are shown as open circles, and 2σ upper limits are marked by upward pointing arrows. The dashed line shows the thermalized value $r_{\rm j1} = 1$. We include literature values of unlensed SMGs and SFGs with CO(1–0) detections. We find no significant correlation for these variables with either ratio.

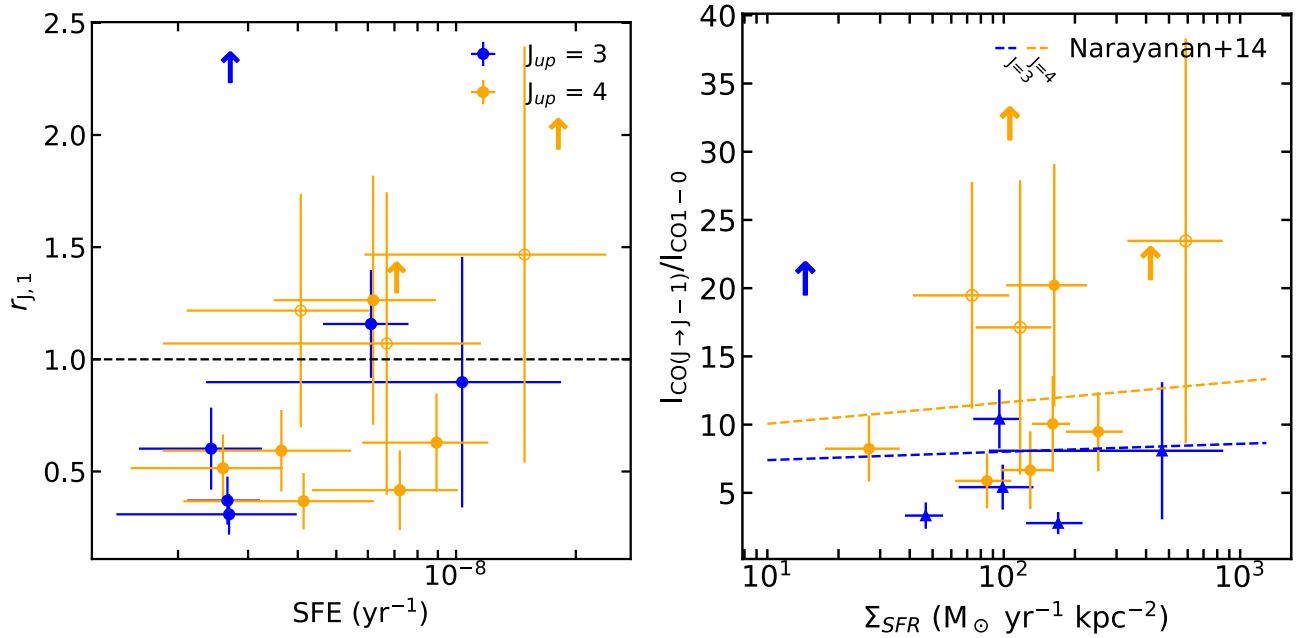

Figure 10. CO(3–2)/CO(1–0) (blue) and CO(4–3)/CO(1–0) (orange) excitation ratios as a function of SFE (left) and SFR surface density (right). Open circles indicate tentative detections, while upward pointing arrows indicate 2σ upper limits. We calculate Pearson's and Spearman's correlation coefficients to look for monotonic trends for these variables and find no significant correlation with SFE. The Spearman's test does reveal a positive correlation of r_{41} with Σ_{SFR}, with a p-value of 0.02, although we are limited by the small sample size and the lack of literature data. Compared to the line excitation predictions from Narayanan & Krumholz (2014) (dashed lines), our sources show a large amount of scatter around the models.

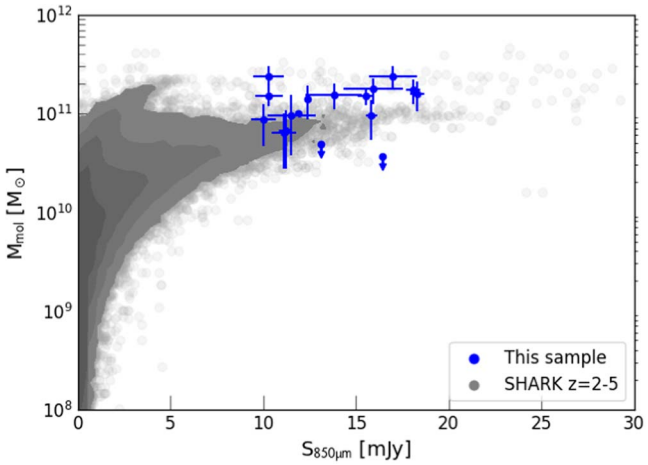

Figure 11. Comparison of 850 μm flux density and M_{mol} between our sample (blue) and $z = 2$–5 galaxies from the SHARK semi-analytic model (gray). We find reasonable agreement between SHARK predictions and our observations (assuming $\alpha_{CO} = 1.0$).

upper envelope of SHARK predictions. This might be a result of an observational bias: SMGs with lower f_{gas} will be fainter in mid-J CO emission and thus more difficult to confirm spectroscopically. However, we note that the spectral survey of Birkin et al. (2021) shows ~75% detection rate; it is thus unlikely that we are missing a substantial population of 850 μm bright, gas-poor SMGs. We note that our choice of $\alpha_{CO} = 1$ for converting the CO(1–0) luminosity to M_{mol} facilitates the agreement between SHARK predictions and our observations: for $\alpha_{CO} \approx 4$, SHARK would have underestimated M_{mol} by a factor of a few.

Figure 12 shows a more detailed comparison with $z = 2$–5 SHARK SMGs with $S_{850} \geqslant 10$ mJy; the SHARK sample totals 1152 galaxies with a median redshift of 2.53. In the $M_\star$–M_{mol} plane, we see a generally good agreement between gas fractions of SHARK SMGs and our sample. Similar to Figure 11, at $M_\star \leqslant 10^{11}$ $M_\odot$, our observations probe the upper end of molecular gas masses predicted by SHARK. Finally, we compare our data and SHARK SMGs in the SFR–M_{mol} plane (Figure 12, right), although there are systematic differences due to the assumption made in SHARK. Namely, SHARK assumes two modes of star formation: a *normal* mode with $t_{dep} = 1$ Gyr, and a *burst* mode with $t_{dep} = 100$ Myr. Despite this limitation, we find a good agreement with our observations, which imply $t_{dep} \approx 50$–400 Myr, with a median of ≈140 Myr (see Section 4.2).

The good agreement between our sample and its SHARK counterparts highlights the power of the state-of-art simulations to reproduce the bulk properties of the SMG population. In particular, as the SHARK model is not tuned to reproduce high-redshift galaxy population, the fact that it reproduces the key properties of the massive end of the SMG population is a remarkable achievement.

5. Conclusions

We have presented new, deep VLA observations of the CO(1–0) emission in 17 dusty SFGs at $z = 2$–4 from the ongoing VLA Legacy Survey of Molecular Gas at High Redshift. We have successfully detected CO(1–0) in 11 sources, with three further tentative detections. These systems are representative of the most massive, SFGs at their redshift. Our main findings are as follows:

1. Our galaxies have total molecular gas masses in the range of 6–23 $\times 10^{10}$ $M_\odot$, assuming a CO-to-H_2 conversion factor of 1. Combined with stellar masses and SFRs obtained via SED fitting, we find a median f_{gas} of 0.35 ± 0.21 and a median t_{dep} of 140 ± 70 Myr. These values are below what would be expected from empirical

Table 4
List of High-redshift Non-lensed SMGs with CO(1–0) Detections and Available Parameters Used in the Figures in This Work

Name	z	$L'_{\mathrm{CO(1-0)}}$ ($\times 10^{10}$) (K km s^{-1} pc^{-2})	FWHM $_{\mathrm{CO(1-0)}}$ (km s^{-1})	r_{31}	r_{41}	SFR ($M_\odot$ yr^{-1})	M_* ($\times 10^{10}$) ($M_\odot$)	f_{gas}	t_{dep} (Myr)	References
ALESS122.2	2.02	13 ± 2	700 ± 60	0.77 ± 0.19	⋯	700 ± 200	8 ± 5	$0.62 \pm$	$140 \pm$	[1], [2], [3]
ALESS67.1	2.12	10 ± 2	710 ± 90	1.01 ± 0.36	⋯	400 ± 100	24 ± 21	$0.29 \pm$	$130 \pm$	[2], [3]
J123549+6215	2.202	8 ± 1	600 ± 50	0.56 ± 0.1	⋯	630 ± 100	21 ± 6	$0.27 \pm$	$123 \pm$	[4], [5]
J16350+4057	2.385	8 ± 1	710 ± 50	0.75 ± 0.13	⋯	1995 ± 100	14 ± 4	$0.37 \pm$	$41 \pm$	[4], [5]
J123707+6214	2.452	11 ± 2	800 ± 50	0.54 ± 0.12	⋯	1000 ± 100	13 ± 3	$0.45 \pm$	$108 \pm$	[4], [6]
J14009+0252	2.486	10 ± 1	434 ± 90	0.38 ± 0.07	⋯	500 ± 250	16 ± 4	$0.38 \pm$	$160 \pm$	[7], [8]
SB1	2.494	4.9 ± 0.4	550 ± 40	0.84 ± 0.07	⋯	1300 ± 120	9 ± 2	0.70 ± 0.1	150 ± 20	[9]
MS1	2.503	2.3 ± 0.2	500 ± 50	0.76 ± 0.07	⋯	290 ± 128	23 ± 2	0.29 ± 0.1	320 ± 140	[9]
MS2	2.507	1.8 ± 0.3	680 ± 90	0.44 ± 0.08	⋯	300 ± 179	22 ± 2	0.25 ± 0.1	250 ± 150	[9]
SB2	2.512	3.2 ± 0.3	340 ± 20	0.78 ± 0.08	⋯	750 ± 340	7 ± 2	0.66 ± 0.1	180 ± 80	[9]
HXMM05	2.985	27 ± 9	1100 ± 300	0.76 ± 0.28	⋯	2900 ± 750	12 ± 7	0.2 ± 0.2	72 ± 27	[10]
J22174+0015	3.099	4 ± 1	560 ± 110	0.79 ± 0.29	⋯	⋯	⋯	⋯	⋯	[11], [12], [13]
J13120+4242	3.408	10 ± 3	267 ± 64	⋯	0.56 ± 0.20	950 ± 420	65 ± 25	0.17 ± 0.03	137 ± 69	[14], [11]
GN20	4.05	16 ± 0.4	670	⋯	0.45 ± 0.12	3000	23	0.4	50	[15],[16]

Note. References are as follows: [1] Huynh et al. (2017), [2] Rivera et al. (2018),[3] Cunha et al. (2015), [4] Ivison et al. (2011), [5] Tacconi et al. (2006), [6] Riechers et al. (2011a),[7] Thomson et al. (2012), [8] Weiß et al. (2009), [9] Xiao et al. (2022), [10] Leung et al. (2019), [11] Greve et al. (2005), [12] Bothwell et al. (2013), [13] Sharon et al. (2016), [14] Frias Castillo et al. (2022), [15] Carilli et al. (2010), [16] Daddi et al. (2009).

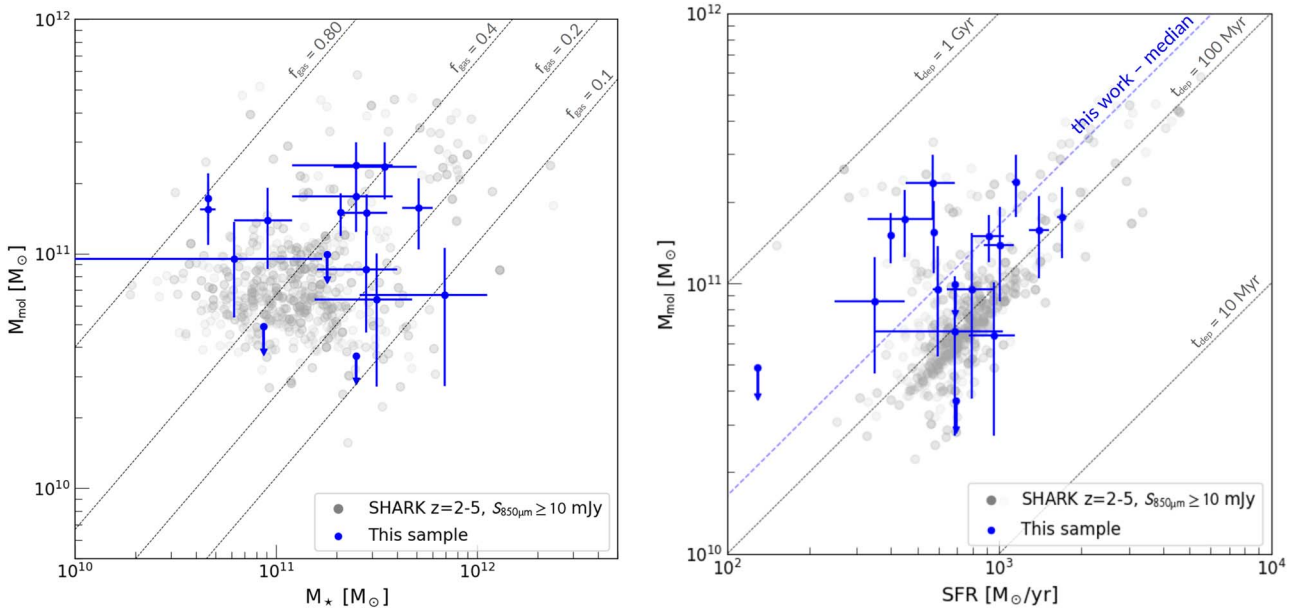

Figure 12. Comparison of our sample with SHARK $z = 2$–5 SMGs with $S_{850} \geqslant 10$ mJy. In the $M_\star$–M_{mol} plane (left), our observations yield M_{mol} on the upper end of the SHARK distribution. The SFR–M_{mol} plane (right) reveals a clear discrepancy in molecular gas depletion timescale t_{dep}: while SHARK assumes a fixed $t_{dep} = 100$ Myr in the *starburst* mode (notice the conspicuous diagonal trend in the model points), we find a median $t_{dep} = 140$ Myr. Despite this limitation, we find a good agreement with our observations, which show a median of ≈140 Myr.

scaling relations, but are consistent with median values found in large surveys of SMGs with mid-J CO observations. We do not see evidence of evolution of f_{gas} or t_{dep} with redshift.

2. Combining our data with ALMA and NOEMA CO(J = 3–2) and CO(J = 4–3) observations yield median excitation ratios of $r_{31} = 0.75 \pm 0.39$ and $r_{41} = 0.63 \pm 0.44$, although there is significant scatter within the sample.
3. We supplement our sample with available literature data of unlensed SMGs, and quantitatively investigate the correlation of the excitation ratios with a number of parameters (e.g., z, CO(1–0) line width, SFE, Σ_{SFR}). We find no significant trends with any of these parameters, except for a tentative positive correlation between r_{41} and Σ_{SFR} for our sources, although we are limited by the sample size. A more in-depth analysis will be available when the full sample has been observed.
4. Finally, we compare our data with the population of $S_{850} > 10$ mJy SMGs from the SHARK catalogs (Lagos et al. 2018). The gas fractions and depletion times of our source show a remarkably good agreement with those of their SHARK counterparts, highlighting the power of current state-of-the-art simulations and their potential synergy with future CO(1–0) surveys of high-redshift galaxies.

Our results highlight the heterogeneous nature of the most massive, SFGs at $z \sim 2.5$–4, and the importance of CO(1–0) observations to robustly constrain their ISM properties. Almost 60% completed, the VLA Legacy Survey of Molecular Gas at High Redshift already provides the basis for follow-up studies, such as the high-resolution VLA CO(1–0) imaging necessary for detailed morphological and dynamical studies, which are currently limited to a handful of the most extreme cases (e.g., Hodge et al. 2012; Frias Castillo et al. 2022).

The National Radio Astronomy Observatory is a facility of the National Science Foundation operated under cooperative agreement by Associated Universities, Inc. M.F.C. and J.A.H. acknowledge the support of the VIDI research program under project number 639.042.611, which is (partly) financed by the Netherlands Organization for Scientific Research (NWO). M.R. is supported by the NWO Veni project "Under the lens" (VI. Veni.202.225). I.R.S., J.E.B., and A.M.S. acknowledge support from STFC (ST/T000244/1). J.E.B. acknowledges the support of STFC studentship (ST/S50536/1). C.-C.C. and C.-L.L. acknowledge support from the National Science and Technology Council of Taiwan (NSTC 109-2112-M-001-016-MY3 and 111-2112-M-001-045-MY3), as well as Academia Sinica through the Career Development Award (AS-CDA-112-M02). Funded by the Deutsche Forschungsgemeinschaft (DFG, German Research Foundation) under Germany's Excellence Strategy EXC-2094-390783311. H.D. acknowledges financial support from the Agencia Estatal de Investigación del Ministerio de Ciencia e Innovación (AEI-MCINN) under a grant (La evolución de los cúmulos de galaxias desde el amanecer hasta el mediodía cósmico) with reference (PID2019-105776GB-I00/DOI:10.13039/501100011033) and acknowledges support from the ACIISI, Consejería de Economía, Conocimiento y Empleo del Gobierno de Canarias and the European Regional Development Fund (ERDF) under a grant with reference PROID2020010107.

Appendix A
Curve of Growth

We perform a curve-of-growth analysis on the 0th-moment maps to determine the optimal aperture to extract the line fluxes. We extract flux densities from a set of circular apertures of increasing diameter and determine the point at which the flux converges, shown in Figure 13. Some of the fainter sources appear not to converge. This is due to the large-scale noise structures, more prominent due to the low S/N of the

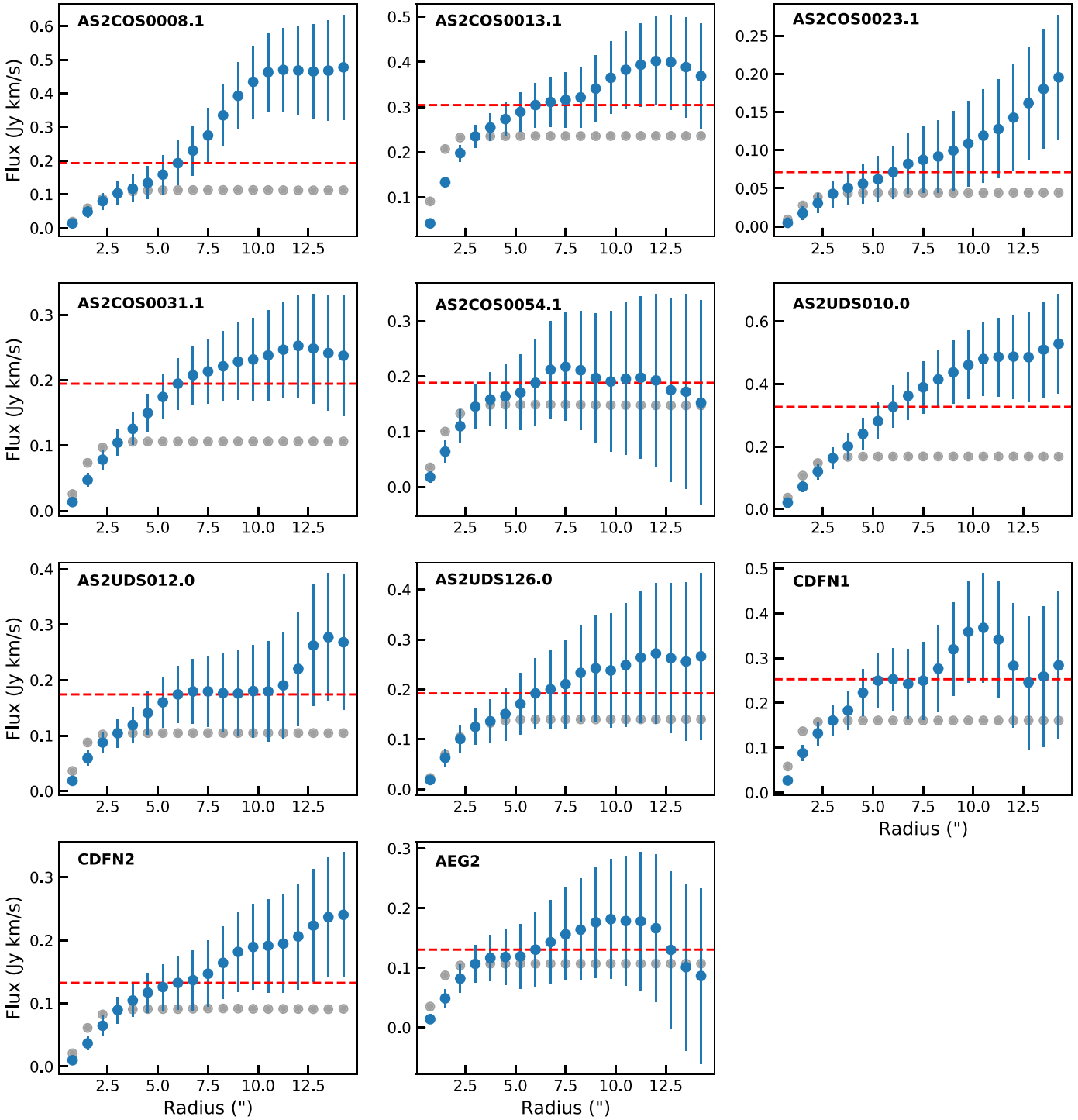

Figure 13. Curve-of-growth analysis performed on the detected sources, showing the flux recovered as a function of aperture radius. The dotted gray line is the curve of growth of the phase calibrator for each source. Compared to the calibrators, some of the brighter sources appear to be extended. The red dashed line marks the flux recovered within a 6″ radius aperture, where most of the sources converge. However, some of the fainter sources appear not to converge, which might be due to large-scale noise structures, more prominent due to the low S/N of the detections (Novak et al. 2020; Chen et al. 2022). Because of this, for the sources with integrated S/N < 3, we extract the flux from an aperture 2.″5 in diameter and then correct it to the total flux based on the median curve of growth. These are AS2COS0008.1, AS2COS0023.1, AS2COS0054.1, AS2UDS126.0, AEG2, and CDFN8.

detections, which has also been observed in other data (Novak et al. 2020; Chen et al. 2022). We note that many of the brighter sources appear to be resolved compared to the phase calibrators, and show extended emission on roughly 6″ radius scales.

Appendix B
Non-detections

Spectra and 0th-moment maps of AS2COS0009.1, AS2UDS014.0 and AEG3 (Figure 14). We do not detect any emission below the 1σ level for these sources.

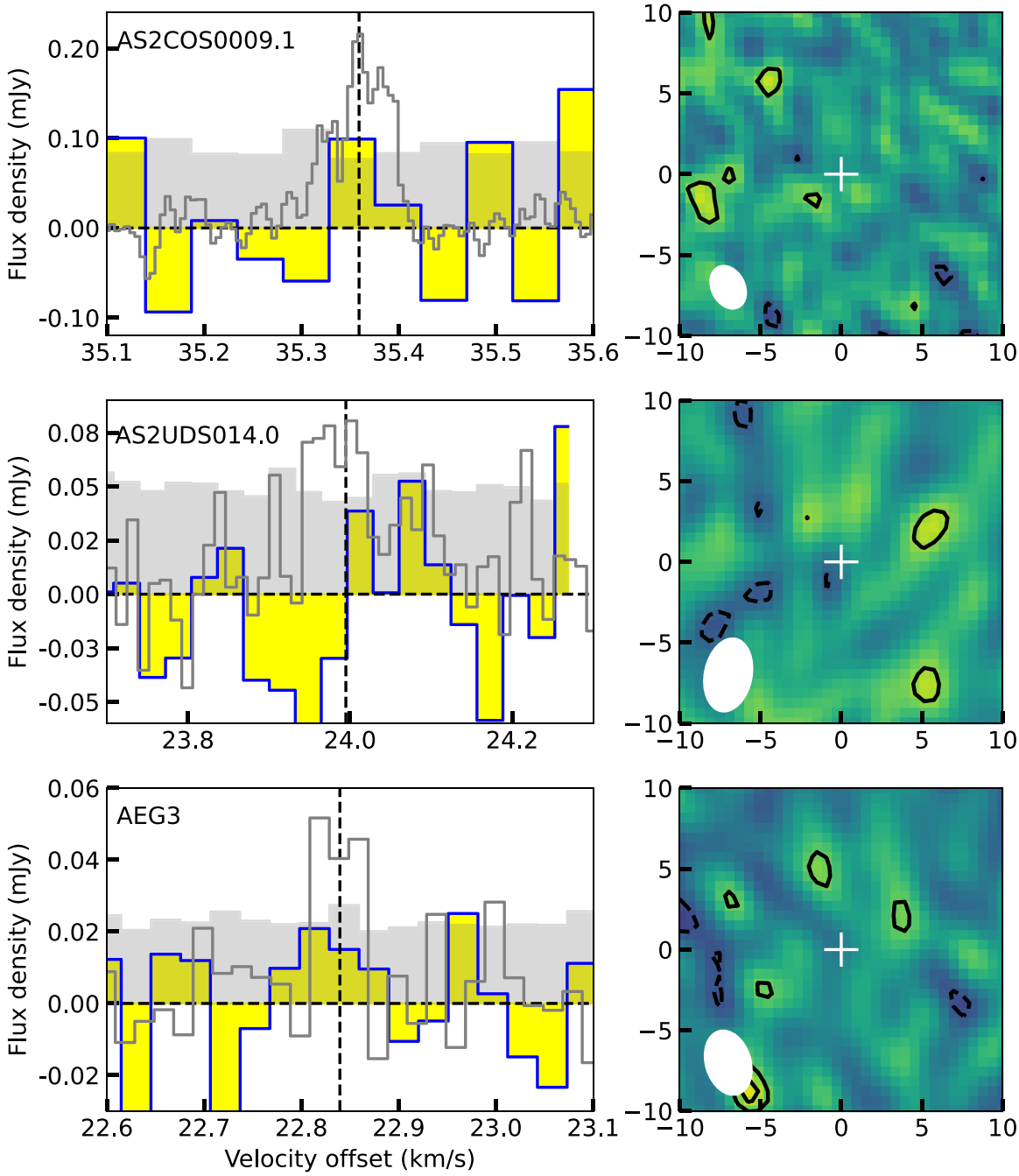

Figure 14. CO(1–0) spectra and 0th-moment maps of the three non-detections, AS2COS0009.1, AS2UDS014.0, and AEG3. The shaded region indicates the 1σ rms per channel and the vertical dashed line indicates the expected redshift of the line based on the existing mid-*J* CO line detections (shown by the gray spectra). To create the maps, we collapsed the data cubes over the line width of their corresponding mid-*J* CO transition. Contours start at 2σ and increase in steps of 1σ. The white cross marks the position of the peak emission of the mid-*J* CO transition. The white ellipse indicates the FWHM of the beam.

ORCID iDs

Marta Frias Castillo https://orcid.org/0000-0002-9278-7028
Jacqueline Hodge https://orcid.org/0000-0001-6586-8845
Matus Rybak https://orcid.org/0000-0002-1383-0746
Paul van der Werf https://orcid.org/0000-0001-5434-5942
Ian Smail https://orcid.org/0000-0003-3037-257X
Jack E. Birkin https://orcid.org/0000-0002-3272-7568
Chian-Chou Chen https://orcid.org/0000-0002-3805-0789
Scott C. Chapman https://orcid.org/0000-0002-8487-3153
Claudia del P.Lagos https://orcid.org/0000-0003-3021-8564
Cheng-Lin Liao https://orcid.org/0000-0002-5247-6639
Elisabete da Cunha https://orcid.org/0000-0001-9759-4797
Gabriela Calistro Rivera https://orcid.org/0000-0003-0085-6346
Jianhang Chen https://orcid.org/0000-0003-3921-3313
E. F. Jiménez-Andrade https://orcid.org/0000-0002-2640-5917
Eric J. Murphy https://orcid.org/0000-0001-7089-7325
Douglas Scott https://orcid.org/0000-0002-6878-9840
A. M. Swinbank https://orcid.org/0000-0003-1192-5837
Fabian Walter https://orcid.org/0000-0003-4793-7880
R. J. Ivison https://orcid.org/0000-0001-5118-1313
Helmut Dannerbauer https://orcid.org/0000-0001-7147-3575

References

Aravena, M., Murphy, E. J., Aguirre, J. E., et al. 2013, MNRAS, 433, 498
Ashby, M. L. N., Willner, S. P., Fazio, G. G., et al. 2015, ApJS, 218, 33
Barro, G., Kriek, M., Pérez-González, P. G., et al. 2016, ApJL, 827, L32
Battisti, A. J., da Cunha, E., Grasha, K., et al. 2019, ApJ, 882, 61
Birkin, J. E., Weiss, A., Wardlow, J. L., et al. 2021, MNRAS, 501, 3926
Bolatto, A. D., Jackson, J. M., Israel, F. P., Zhang, X., & Kim, S. 2000, ApJ, 545, 234
Bolatto, A. D., Leroy, A., Israel, F. P., & Jackson, J. M. 2003, ApJ, 595, 167
Bolatto, A. D., Wolfire, M., & Leroy, A. K. 2013, ARA&A, 51, 207
Boogaard, L. A., Werf, P. v. d., Weiss, A., et al. 2020, ApJ, 902, 109
Bothwell, M. S., Smail, I., Chapman, S. C., et al. 2013, MNRAS, 429, 3047
Carilli, C. L., Daddi, E., Riechers, D., et al. 2010, ApJ, 714, 1407
Carilli, C. L., & Walter, F. 2013, ARA&A, 51, 105
Casey, C. M., Narayanan, D., & Cooray, A. 2014, PhR, 541, 45
Chapman, S. C., Blain, A. W., Smail, I., & Ivison, R. J. 2005, ApJ, 622, 772
Chen, C.-C., Liao, C.-L., Smail, I., et al. 2022, ApJ, 929, 159
Cunha, E. d., Walter, F., Smail, I. R., et al. 2015, ApJ, 806, 110
da Cunha, E., Groves, B., Walter, F., et al. 2013, ApJ, 766, 13
Daddi, E., Dannerbauer, H., Liu, D., et al. 2015, A&A, 577, A46
Daddi, E., Dannerbauer, H., Stern, D., et al. 2009, ApJ, 694, 1517
Danielson, A. L. R., Swinbank, A. M., Smail, I., et al. 2011, MNRAS, 410, 1687
Danielson, A. L. R., Swinbank, A. M., Smail, I., et al. 2017, ApJ, 840, 78
Dannerbauer, H., Lehnert, M. D., Emonts, B., et al. 2017, A&A, 608, A48
Davé, R., Anglés-Alcázar, D., Narayanan, D., et al. 2019, MNRAS, 486, 2827
Decarli, R., Aravena, M., Boogaard, L., et al. 2020, ApJ, 902, 110
Decarli, R., Walter, F., Gónzalez-López, J., et al. 2019, ApJ, 882, 138
Dudzeviciute, U., Smail, I., Swinbank, A. M., et al. 2020, MNRAS, 494, 3828
Elahi, P. J., Welker, C., Power, C., et al. 2018, MNRAS, 475, 5338
Elbaz, D., Dickinson, M., Hwang, H. S., et al. 2011, A&A, 533, A119
Emonts, B. H. C., Lehnert, M. D., Villar-Martín, M., et al. 2016, Sci, 354, 1128
Frayer, D. T., Maddalena, R. J., Ivison, R. J., et al. 2018, ApJ, 860, 87
Frias Castillo, M., Rybak, M., Hodge, J., et al. 2022, ApJ, 930, 35
Geach, J. E., Dunlop, J. S., Halpern, M., et al. 2017, MNRAS, 465, 1789
Genzel, R., Tacconi, L. J., Lutz, D., et al. 2015, ApJ, 800, 20
Greve, T. R., Bertoldi, F., Smail, I., et al. 2005, MNRAS, 359, 1165
Greve, T. R., Leonidaki, I., Xilouris, E. M., et al. 2014, ApJ, 794, 142
Gullberg, B., Smail, I., Swinbank, A. M., et al. 2019, MNRAS, 490, 4956
Harrington, K. C., Weiss, A., Yun, M. S., et al. 2021, ApJ, 908, 95
Harrington, K. C., Yun, M. S., Magnelli, B., et al. 2018, MNRAS, 474, 3866
Harris, A. I., Baker, A. J., Frayer, D. T., et al. 2012, ApJ, 752, 152
Hayward, C. C., Kereš, D., Jonsson, P., et al. 2011, ApJ, 743, 159
Hildebrand, R. H. 1983, QJRAS, 24, 267
Hill, R., Chapman, S. C., Scott, D., et al. 2018, MNRAS, 477, 2042
Hodge, J. A., Carilli, C. L., Walter, F., et al. 2012, ApJ, 760, 11
Hodge, J. A., & da Cunha, E. 2020, RSOS, 7, 200556
Hodge, J. A., Smail, I., Walter, F., et al. 2019, ApJ, 876, 130
Hodge, J. A., Swinbank, A. M., Simpson, J. M., et al. 2016, ApJ, 833, 103
Huynh, M. T., Emonts, B. H. C., Kimball, A. E., et al. 2017, MNRAS, 467, 1222
Ikarashi, S., Ivison, R. J., Caputi, K. I., et al. 2015, ApJ, 810, 133
Ivison, R. J., Papadopoulos, P. P., Smail, I., et al. 2011, MNRAS, 412, 1913
Ivison, R. J., Smail, I., Papadopoulos, P. P., et al. 2010, MNRAS, 404, 198
Jarugula, S., Vieira, J. D., Weiss, A., et al. 2021, ApJ, 921, 97
Kaasinen, M., Scoville, N., Walter, F., et al. 2019, ApJ, 880, 15
Kennicutt, R. C., & Evans, N. J. 2012, ARA&A, 50, 531
Kennicutt, R. C., Jr 1998, ApJ, 498, 541
Lagos, C. d. P., da Cunha, E., Robotham, A. S. G., et al. 2020, MNRAS, 499, 1948
Lagos, C. d. P., Robotham, A. S. G., Trayford, J. W., et al. 2019, MNRAS, 489, 4196
Lagos, C. d. P., Tobar, R. J., Robotham, A. S. G., et al. 2018, MNRAS, 481, 3573
Lee, B., Giavalisco, M., Whitaker, K., et al. 2018, ApJ, 853, 131
Leslie, S. K., Schinnerer, E., Liu, D., et al. 2020, ApJ, 899, 58
Leung, T. K. D., Riechers, D. A., Baker, A. J., et al. 2019, ApJ, 871, 85
Liang, L., Feldmann, R., Faucher-Giguere, C.-A., et al. 2018, MNRAS, 478, L83
Liu, D., Schinnerer, E., Groves, B., et al. 2019, ApJ, 887, 235
Lovell, C. C., Geach, J. E., Davé, R., Narayanan, D., & Li, Q. 2021, MNRAS, 502, 772
Magnelli, B., Lutz, D., Santini, P., et al. 2012, A&A, 539, A155
McAlpine, S., Smail, I., Bower, R. G., et al. 2019, MNRAS, 488, 2440
McMullin, J. P., Waters, B., Schiebel, D., Young, W., & Golap, K. 2007, in ASP Conf. Ser. 376, Astronomical Data Analysis Software and Systems XVI, ed. R. A. Shaw, F. Hill, & D. J. Bell (San Francisco, CA: ASP), 127
Narayanan, D., Bothwell, M., & Dave, R. 2012, MNRAS, 426, 1178
Narayanan, D., & Krumholz, M. R. 2014, MNRAS, 442, 1411
Novak, M., Venemans, B. P., Walter, F., et al. 2020, ApJ, 904, 131
Oliver, S. J., Bock, J., Altieri, B., et al. 2012, MNRAS, 424, 1614
Papadopoulos, P. P., van der Werf, P. P., Xilouris, E. M., et al. 2012, MNRAS, 426, 2601
Pavesi, R., Sharon, C. E., Riechers, D. A., et al. 2018, ApJ, 864, 49
Planck Collaboration, Ade, P. A. R., Aghanim, N., et al. 2016, A&A, 594, A13
Riechers, D. A., Boogaard, L. A., Decarli, R., et al. 2020, ApJL, 896, L21
Riechers, D. A., Carilli, L. C., Walter, F., et al. 2011a, ApJL, 733, L11
Riechers, D. A., Hodge, J., Walter, F., Carilli, C. L., & Bertoldi, F. 2011b, ApJL, 739, L31
Riechers, D. A., Pavesi, R., Sharon, C. E., et al. 2019, ApJ, 872, 7
Rivera, G. C., Hodge, J. A., Smail, I., et al. 2018, ApJ, 863, 56
Schaye, J., Crain, R. A., Bower, R. G., et al. 2015, MNRAS, 446, 521
Schreiber, C., Pannella, M., Elbaz, D., et al. 2015, A&A, 575, A74
Scoville, N., Sheth, K., Aussel, H., et al. 2016, ApJ, 820, 83
Sharon, C. E., Riechers, D. A., Hodge, J., et al. 2016, ApJ, 827, 18
Simpson, J. M., Smail, I., Dudzevičiūtė, U., et al. 2020, MNRAS, 495, 3409
Simpson, J. M., Smail, I., Swinbank, A. M., et al. 2015, ApJ, 799, 81
Simpson, J. M., Smail, I., Swinbank, A. M., et al. 2019, ApJ, 880, 43
Solomon, P. M., & Vanden Bout, P. A. 2005, ARA&A, 43, 677
Speagle, J. S., Steinhardt, C. L., Capak, P. L., & Silverman, J. D. 2014, ApJS, 214, 15
Stach, S. M., Dudzevičiūtė, U., Smail, I., et al. 2019, MNRAS, 487, 4648
Stach, S. M., Smail, I., Swinbank, A. M., et al. 2018, ApJ, 860, 161
Tacconi, L. J., Genzel, R., Saintonge, A., et al. 2018, ApJ, 853, 179
Tacconi, L. J., Genzel, R., Smail, I., et al. 2008, ApJ, 680, 246
Tacconi, L. J., Genzel, R., & Sternberg, A. 2020, ARA&A, 58, 157
Tacconi, L. J., Neri, R., Chapman, S. C., et al. 2006, ApJ, 640, 228
Thomson, A. P., Ivison, R. J., Smail, I., et al. 2012, MNRAS, 425, 2203
Valentino, F., Daddi, E., Puglisi, A., et al. 2020, A&A, 641, A155
Valentino, F., Magdis, G. E., Daddi, E., et al. 2018, ApJ, 869, 27
van der Werf, P. P., Isaak, K. G., Meijerink, R., et al. 2010, A&A, 518, L42
Walter, F., Decarli, R., Aravena, M., et al. 2016, ApJ, 833, 67
Walter, F., Weiß, A., Downes, D., Decarli, R., & Henkel, C. 2011, ApJ, 730, 18
Wang, S. X., Brandt, W. N., Luo, B., et al. 2013, ApJ, 778, 179
Wang, T.-M., Magnelli, B., Schinnerer, E., et al. 2022, A&A, 660, A142
Wang, W.-H., Cowie, L. L., Barger, A. J., Keenan, R. C., & Ting, H.-C. 2010, ApJS, 187, 251
Weiß, A., Downes, D., Walter, F., & Henkel, C. 2005, A&A, 440, L45
Weiß, A., Ivison, R. J., Downes, D., et al. 2009, ApJL, 705, L45
Whitaker, K. E., Franx, M., Leja, J., et al. 2014, ApJ, 795, 104
Xiao, M.-Y., Wang, T., Elbaz, D., et al. 2022, A&A, 664, A63
Yang, C., Omont, A., Beelen, A., et al. 2017, A&A, 608, A144
Yao, L., Seaquist, E. R., Kuno, N., & Dunne, L. 2003, ApJ, 588, 771